Lagrange Wavelets for Signal Processing

Zhuoer Shi, *Member, IEEE*, G. W. Wei, Donald J. Kouri, *Member, IEEE*, David K. Hoffman, and Zheng Bao, *Senior Member, IEEE*

***Abstract*—This paper deals with the design of interpolating wavelets based on a variety of Lagrange functions, combined with novel signal processing techniques for digital imaging. Halfband Lagrange wavelets, B-spline Lagrange wavelets and Gaussian Lagrange [Lagrange distributed approximating functional (DAF)] wavelets are presented as specific examples of the generalized Lagrange wavelets. Our approach combines the perceptually dependent visual group normalization (VGN) technique and a softer logic masking (SLM) method. These are utilized to rescale the wavelet coefficients, remove perceptual redundancy and obtain good visual performance for digital image processing.**

***Index Terms*—Distributed approximating functionals, generalized Lagrange wavelets, softer logic masking, visual group normalization.**

I. Introduction

THE theory of interpolating wavelets has attracted much attention recently [1], [9], [11]–[13], [20]–[22], [29], [30], [33]–[37], [45], [46]. It possesses the attractive characteristic that the wavelet coefficients are obtained from the direct linear combinations of discrete samples rather than from the traditional inner product integrals. Mathematically, various interpolating wavelets can be formulated in an orthogonal or biorthogonal setting. Harten has described a kind of piecewise biorthogonal wavelet construction [13]. Swelden independently has developed essentially this method into the “lifting scheme” [37], which can be regarded as a special case of the Neville filters [21]. Unlike the previous method for constructing biorthogonal wavelets, which relies on explicit solution of coupled algebraic equations [5]–[7], the lifting scheme enables one to construct custom-designed biorthogonal wavelet transforms assuming only a single low-pass filter, without iteration. Generally speaking, the lifting-interpolating wavelet theory is closely related to the finite element technique for the numerical solution of partial differential equations, the subdivision scheme for interpolation and approximation, multigrid generation and surface fitting techniques. The most attractive feature of the approach is that the discrete samplings are identical to wavelet multiresolution analysis. Without any pre-conditioning or post-processing that was required previously for an accurate wavelet analysis, the interpolating wavelet coefficients can be implemented using a parallel computational scheme.

Lagrange interpolation polynomials are commonly used for signal approximation and smoothing. By carefully designing the interpolating Lagrange functionals, one can obtain smooth interpolating scaling functions with arbitrary finite order of regularity. In this paper, we present three different kinds of biorthogonal interpolating Lagrange wavelets (Halfband Lagrange wavelets, B-spline Lagrange wavelets and Gaussian Lagrange (LDAF) wavelets) as specific examples of generalized *Lagrange wavelets*. *Halfband Lagrange wavelets* can be regarded as an extension of Dubuc interpolating functionals [9], [12], auto-correlation shell[1] wavelet analysis [29], and halfband filters [1]. *B-spline Lagrange Wavelets* are generated by a B-spline-windowed Lagrange functional which increases the smoothness and localization properties of the simple Lagrange scaling function and related wavelets. *Lagrange DAFs*, generated using Gaussian windowed Lagrange polynomials, have been successfully used for numerically solving various linear and nonlinear partial differential equations [45]. Typical examples include DAF-simulations of 3D reactive quantum scattering and 2D Navier–Stokes fluid flow with nonperiodic boundary conditions. In terms of wavelet analysis, DAFs can be regarded as particular scaling functions (wavelet-DAFs); the associated DAF-wavelets are generated in a number of ways [34]–[36]. Both DAFs and DAF-wavelets are smooth and decay rapidly in both the time and frequency representations. One objective of the present work is to construct new biorthogonal DAF-wavelets and the associated DAF-filters.

As an example application to illustrate Lagrange wavelets, we consider image processing. This application typically requires dealing with very large data sets, complicated space-frequency distributions and complex, perceptual dependent characteristics. Denoising and restoration play an important role in image processing. Noise distortion not only affects the visual quality of images, but also degrades the efficiency of data compression and coding. To exploit the time-frequency characteristics of wavelets, an earlier *group normalization* (GN) technique [31], [32] has been introduced to re-scale the wavelet coefficients. The group normalization procedure corrects the defect that the wavelet coefficient magnitudes do not correctly reflect

Manuscript received May 12, 1998; revised June 14, 2001. This work was supported by the National Science Foundation under Grant CHE-9700297, the R. A. Welch Foundation under Grant E-0608, the Department of Energy under Contract 2-7405-ENG82, the NSERC of Canada, and the Chinese National Science Foundation under Grant 69572031.

Z. Shi and D. J. Kouri are with the Department of Physics, University of Houston, Houston, TX 77204 USA (e-mail: zshi@bayou.uh.edu; kouri@uh.edu).

G. W. Wei was with the Department of Physics, University of Houston, Houston, TX 77204 USA. He is now with the Department of Computational Science, National University of Singapore, Singapore 129260 (e-mail: cscweigw@nus.edu.sg).

D. K. Hoffman is with the Department of Chemistry and Ames Laboratory, Iowa State University, Ames, IA 50011 USA (e-mail: hoffman@ameslab.gov).

Z. Bao is with the National Key Laboratory of Radar Signal Processing, Xi’an 710071, China (e-mail: zhbao@rsp.xidian.edu.cn).

Publisher Item Identifier S 1057-7149(01)08798-X.

[1]The term “shell” in this paper refers to a generalized function $\varphi(\cdot)$, whose translation class $\{\varphi(\cdot - k)\}$ constructs a kind of functional approximation for a function $f \in L^2(R)$.

the true strength of the various signal components. In order to achieve the best noise-removing efficiency, the visual response is best accounted for by a *perceptual normalization* procedure based on the characteristics of the *human vision system* (HVS). The concept of visual loss-less quantization [44] is employed to construct the visual loss-less matrix, which re-adjusts the magnitude-normalized coefficients.

Perceptual signal processing has the potential of overcoming the limits of the traditional Shannon Rate-distortion (R-D) theory for perception-dependent information, such as images and acoustic signals. Previously, Ramchandran, Vetterli, Xiong, Herley, Asai, and Orchard have utilized a rate-distortion compromise for image compression [15], [26], [27], and [47]. Our recently derived visual group normalization (VGN) technique [35], [36] can be used with a rate-distortion compromise to generate a so-called *visual rate-distortion* (VR-D) theory to improve image processing further.

As an adjusted denoising technique, softer logic masking (SLM) [32] is designed to improve the filtering performance of Donoho's soft thresholding method [10]. The SLM technique efficiently preserves important information (particularly at an edge transition) in a manner suited to human visual perception. In this paper, the above mentioned approaches are combined with generalized Lagrange wavelets to achieve excellent blind image restoration performance.

II. Interpolating Wavelets

The basic characteristics of interpolating wavelets of order D require that the primary scaling functions satisfy the following conditions [11].

1) Interpolation:

$$\phi(k) = \begin{cases} 1, & k = 0 \\ 0, & k \neq 0, \end{cases} \qquad k \in Z. \tag{1}$$

2) Self-Induced Two-Scale Relation: ϕ can be represented as a linear combination of the dilates and translates of itself, while the weight is the value of ϕ at a subdivision integer of order 2

$$\phi(x) = \sum_k \phi(k/2)\phi(2x - k). \tag{2}$$

This is only approximately satisfied for some of the interpolating wavelets discussed in the later sections; however, the approximation can be made arbitrarily accurate.

3) Polynomial Span: For an integer $D \geq 0$, the collection of formal sums, symbolized by $\Sigma C_k \phi(x-k)$, contains all polynomials of degree D.

4) Regularity: For real $V > 0$, ϕ is Hölder continuous of order V.

5) Localization: ϕ and all its derivatives through order $\lfloor V \rfloor$ decay rapidly

$$\left|\phi^{(r)}(x)\right| \leq A_s(1+|x|)^{-s}, \qquad x \in R, \quad s > 0, \qquad 0 \leq r \leq \lfloor V \rfloor \tag{3}$$

here $\lfloor V \rfloor$ represents the maximum integer which does not exceed V. ■

Interpolating wavelets are particularly efficient for signal representation since their multiresolution analysis is simply realized by discrete sampling. This makes it easy to generate a subband decomposition without requiring tedious iterations. Moreover, adaptive boundary treatments and nonuniform samplings can be easily implemented using interpolating methods. Compared with commonly used wavelet transforms, the interpolating wavelet transform possesses the following characteristics.

1) The wavelet transform coefficients are generated by a linear combination of signal samplings, instead of the commonly used convolution wavelet transform, such as

$$W_{j,k} = \int_R \psi_{j,k}(x) f(x)\, dx \tag{4}$$

where $\psi_{j,k}(x) = 2^{j/2}\psi(2^j x - k)$.

2) A parallel-computing algorithm can be easily constructed. The calculation and compression of coefficients are not coupled. For the halfband filter with length L, the calculation of the wavelet coefficients does not exceed $L+2$ multiply/adds for each coefficient.

3) For a Dth order differentiable function, the wavelet coefficients decay rapidly.

4) In a minimax sense, threshold masking and quantization are nearly optimal for a wide variety of regularization algorithms.

Theoretically, interpolating wavelets are closely related to the following wavelet types.

1) Band-Limited Shannon Wavelets: The π band-limited function, $\phi(x) = \sin(\pi x)/\pi x \in C^\infty$ in Paley–Wiener space, constructs interpolating functions. Every π band-limited function $f \in L^2(R)$ can be reconstructed by the equation

$$f(x) = \sum_k f(k) \frac{\sin \pi(x-k)}{\pi(x-k)} \tag{5}$$

where the related wavelet function (the Sinclet) is defined as (see Fig. 1)

$$\psi(x) = \frac{\sin \pi(2x-1) - \sin \pi(x - 1/2)}{\pi(x-1/2)}. \tag{6}$$

2) Interpolating Cardinal Spline: The cardinal polynomial spline of degree D, $\phi_D(x)$, where D is an odd integer, has been shown to be an interpolating wavelet (see Fig. 2). It is smooth with order $R = D - 1$, and its derivatives through order $D-1$ decay exponentially [39]. Thus

$$\phi_D(x) = \sum_k \alpha_D(k)\beta_D(x-k) \tag{7}$$

where $\beta_D(x)$ is the B-spline of order D defined as

$$\beta_D(x) = \sum_{j=0}^{D+1} \frac{(-1)^j}{D!}\binom{D+1}{j}\left(x + \frac{D+1}{2} - j\right)^D \cdot U\left(x + \frac{D+1}{2} - j\right). \tag{8}$$

Here, U is the step function

$$U(x) = \begin{cases} 0, & x < 0 \\ 1, & x \geq 0 \end{cases} \tag{9}$$

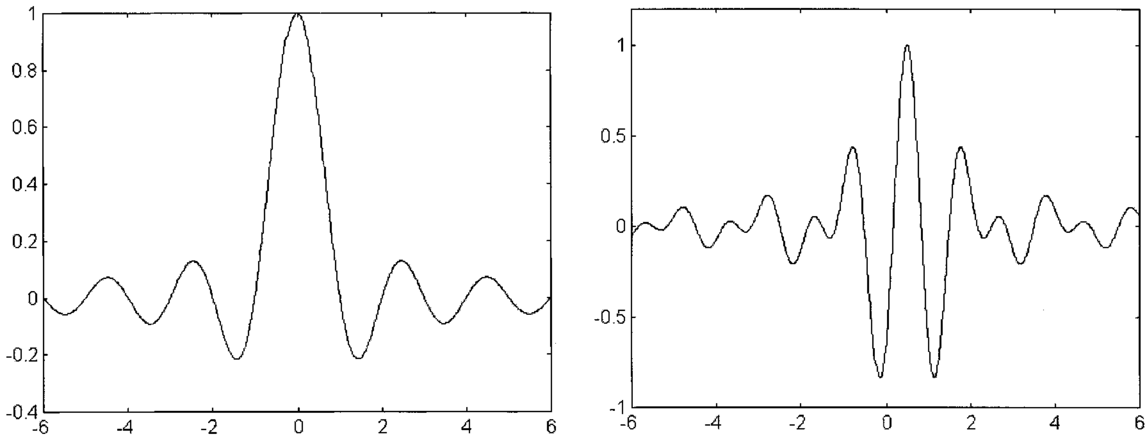

(a) (b)

Fig. 1. π band-limited interpolating wavelets. (a) *Sinc* function and (b) *Sinclet* wavelet.

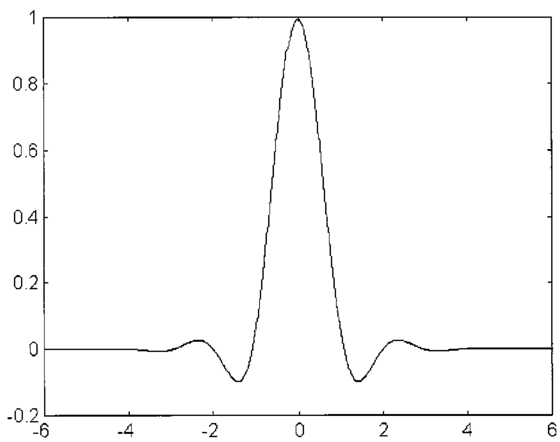

Fig. 2. Interpolating cardinal spline ($D = 5$).

and $\{\alpha_D(k)\}$ is the sequence that satisfies the infinite summation condition

$$\sum_k \alpha_D(k)\beta_D(n-k) = \delta(n). \tag{10}$$

3) Deslauriers–Dubuc Functional: Let D be an odd integer, and $D > 0$. There exist functions, F_D, such that if F_D has already been defined at all binary rationals with denominator 2^j, it can be extended by polynomial interpolation to all binary rationals with denominator 2^{j+1}, i.e., all points halfway between the previously defined points [9], [12]. Specifically, to define the function at $2^{-j-1}(2k+1)$ when it is already defined at all $\{k2^{-j}\}$, fit a polynomial $\pi_{j,k}$ to the data $(k'/2^j, F_D(k'/2^j))$ for $k' \in \{2^{-j}[k-(D-1)/2], \ldots, 2^{-j}[k+(D+1)/2]\}$. This polynomial is unique

$$F_D\left(\frac{k+1/2}{2^j}\right) \equiv \pi_{j,k}\left(\frac{k+1/2}{2^j}\right). \tag{11}$$

This subdivision scheme defines a function that is uniformly continuous at the rationals and has a unique continuous extension. The function F_D is a compactly supported interval polynomial and is regular; it is the auto-correlation function of the Daubechies wavelet [8] of order $D+1$. This function is at least as smooth as the corresponding Daubechies wavelets.

4) Auto-Correlation Shell of Orthonormal Wavelets: If $\breve{\phi}$ is an orthonormal scaling function, its auto-correlation $\phi(x) = \int \breve{\phi}(t)\breve{\phi}(x-t)\,dt$ is an interpolating wavelet (Fig. 3) [29]. Its smoothness, localization and two-scale relations derive from $\breve{\phi}$. The auto-correlation of Haar, Lamarie–Battle, Meyer, and Daubechies wavelets lead, respectively, to the interpolating Schauder, interpolating spline, C^∞ interpolating, and Deslauriers–Dubuc wavelets.

5) Lagrange Half-Band Filters: Ansari *et al.* [1] have used Lagrange symmetric halfband FIR filters to design the orthonomal wavelets that express the relation between the Lagrange interpolators and Daubechies wavelets. Their filter corresponds to the Deslauriers–Dubuc wavelet of order $D = 2M - 1 = 7$, $M = 4$. The transfer function of the halfband symmetric filter h is given by

$$H(z) = \tfrac{1}{2} + zT(z^2) \tag{12}$$

where T is a trigonometric polynomial. Except for $h(0) = 1/2$, at every even integer lattice $h(2n) = 0$, $n \neq 0$, $n \in Z$. The transfer function of the symmetric FIR filter $h(n) = h(-n)$, has the form

$$H(z) = \tfrac{1}{2} + \sum_{n=1}^{M} h(2n-1)(z^{1-2n} + z^{2n-1}). \tag{13}$$

The concept of an interpolating wavelet decomposition is similar to that of "algorithm a trous," the connection having been found by Shensa [30]. Moreover, the interpolating wavelets invoke the construction of wavelet sampling theory. Based on that, Xia *et al.* developed several compactly supported interpolating wavelets [47]. The self-induced scaling conditions and interpolation condition are the most important characteristics of interpolating wavelets. According to the following equation:

$$f(x) = \Sigma_n f(n)\phi(x-n) \tag{14}$$

the signal approximation is exact on the discrete integer sampling points, which does not hold in general for commonly used noninterpolating wavelets.

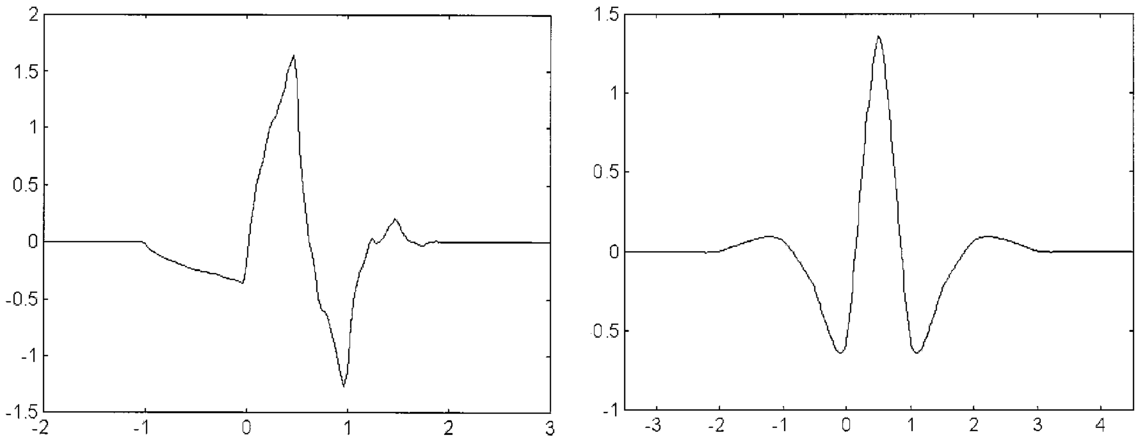

(a) (b)

Fig. 3. Interpolating wavelets by auto-correlation shell ($D = 3$). (a) Daubechies wavelet and (b) Dubuc wavelet.

III. Lagrange Wavelets

A. Halfband Lagrange Wavelets

The halfband filter is defined as one whose even samples of the impulse response are constrained such that $h(0) = 1/2$ and $h(2n) = 0$ for $n = \pm 1, \pm 2, \ldots$ A special case of symmetric halfband filters can be obtained by choosing the filter coefficients according to the Lagrange interpolation formula. The filter coefficients are then given by

$$h(2n-1) = \frac{(-1)^{n+M-1} \prod_{m=1}^{2M} (M + 1/2 - m)}{(M-n)!(M+n-1)!(2n-1)}. \tag{15}$$

These filters have the property of maximal flatness. They possess a balance between the degree of flatness at zero frequency and flatness at the Nyquist frequency (half sampling).

These half-band filters can be utilized to generate the interpolating wavelet decomposition, which is regarded as a class of auto-correlated shells of orthogonal wavelets. The interpolating wavelet transform can also be generated by the following Lagrange polynomials [29]

$$P_{2n-1}(x) = \prod_{m=-M+1,\, m\neq n}^{M} \frac{x-(2m-1)}{(2n-1)-(2m-1)}. \tag{16}$$

In such a case, the predicted interpolation is expressed as

$$\Gamma S_j(i) = \sum_{n=1}^{M} P_{2n-1}(0)[S_j(i+2n-1) + S_j(i-2n+1)], \quad i = 2k+1 \tag{17}$$

where Γ is a projection and S_j are the low-pass coefficients at the jth layer. This projection relation is equivalent to the subband filter response of

$$h(2n-1) = P_{2n-1}(0). \tag{18}$$

The aforementioned interpolating wavelets can be regarded as an extension of the fundamental Deslauriers–Dubuc interactive subdivision scheme (factorized as $M = 2$, while the order of Lagrange polynomial is $D = 2M - 1 = 3$) [Fig. 5(a)].

It is easy to verify that an increase of the Lagrange polynomial order will introduce higher regularity in the interpolating functionals [Fig. 7(a)]. When $D \rightarrow +\infty$, the interpolating functional becomes the π-band-limited Sinc function and its definition domain is the real line. The subband filters generated by Lagrange interpolating functionals satisfy

1) Interpolation: $h(\omega) + h(\omega + \pi) = 1$.
2) Symmetry: $h(\omega) = h(-\omega)$.
3) Vanishing moments: $\int_R x^p \phi(x)\, dx = \delta_p$.

The biorthogonal condition is characterized by [6] as

$$\begin{cases} h(\omega)\overline{\tilde{h}(\omega)} + g(\omega)\overline{\tilde{g}(\omega)} = 1 \\ h(\omega)\overline{\tilde{h}(\omega+\pi)} + g(\omega)\overline{\tilde{g}(\omega+\pi)} = 0. \end{cases} \tag{19}$$

Donoho outlines a basic subband extension for perfect reconstruction. He defines the wavelet function as

$$\psi(x) = \phi(2x - 1). \tag{20}$$

Thus the biorthogonal subband filters are expressed as

$$\tilde{h}(\omega) = 1, \qquad g(\omega) = e^{-i\omega}, \qquad \tilde{g}(\omega) = e^{-i\omega}\overline{h(\omega+\pi)} \tag{21}$$

which satisfies the (19). However, the Donoho interpolating wavelets have some drawbacks, because the low-pass coefficients are generated by a sampling operation only. As the decomposition layer increases, the correlation between low-pass coefficients becomes weaker. The interpolating (prediction) error (high-pass coefficients) strongly increases, which destroys the compact representation of the signal. Additionally, it does not lead to a Riesz basis for $L^2(R)$ space.

Swelden has provided, by far, the most efficient and robust scheme [37] for constructing biorthogonal wavelet filters. His approach generates high-order interpolating Lagrange wavelets

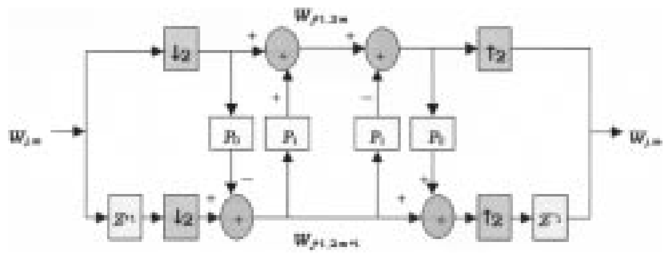

Fig. 4. Lifting scheme.

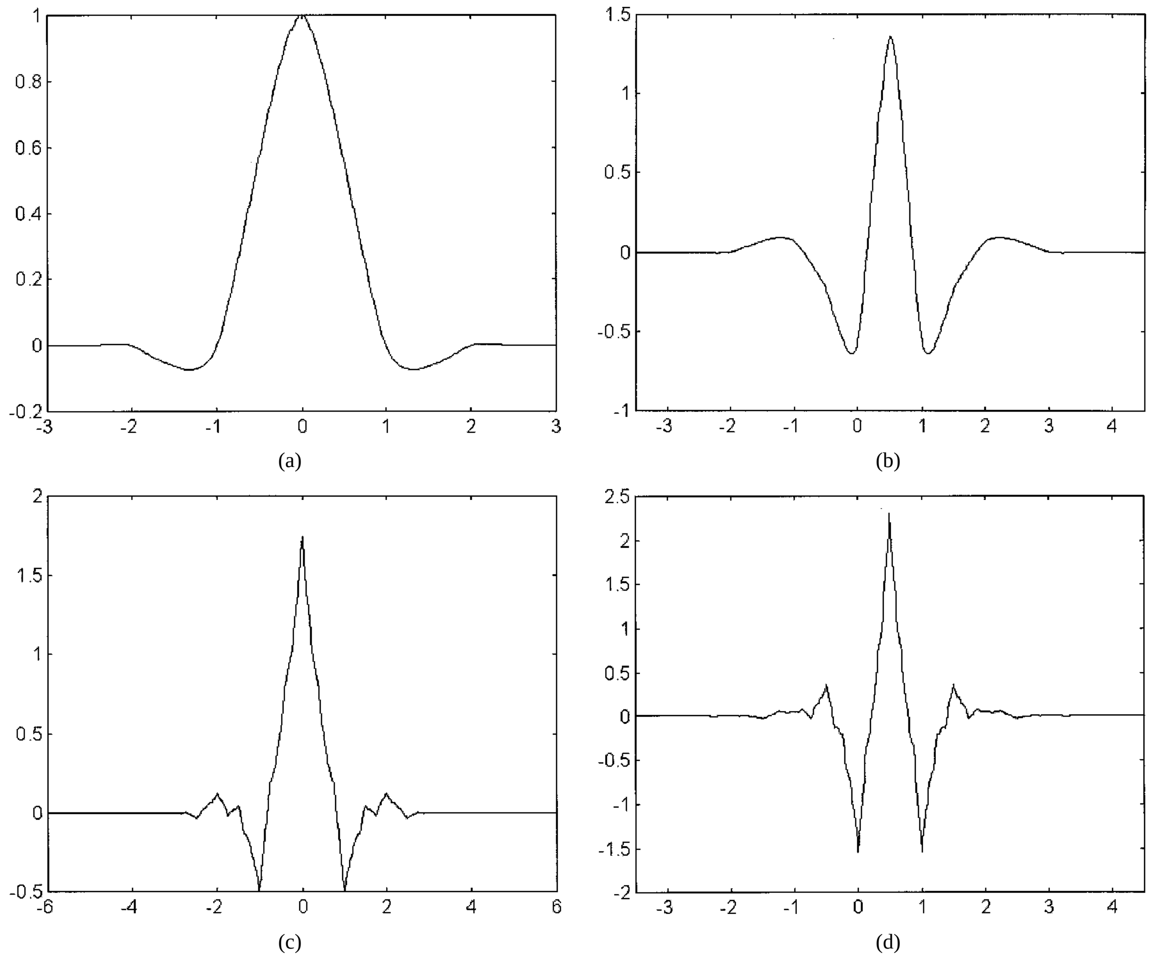

Fig. 5. Lagrange wavelets with order $D = 3$. (a) Scaling, (b) wavelet, (c) dual scaling, and (d) dual wavelet.

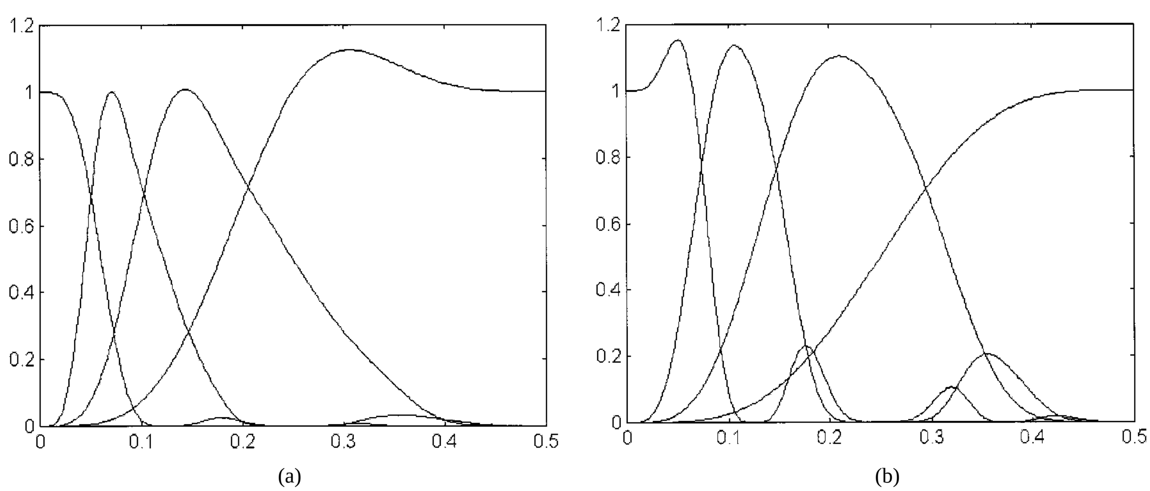

Fig. 6. Frequency response of equivalent filters ($D = 3$, $J = 3$). (a) Decomposition and (b) reconstruction.

with increased regularity. In this case, the interpolating subband filters are

$$\begin{cases} h_1(\omega) = h(\omega) \\ \tilde{h}_1(\omega) = 1 + \tilde{g}(\omega)\overline{P(2\omega)} \\ g_1(\omega) = e^{-i\omega} - h(\omega)P(2\omega) \\ \tilde{g}_1(\omega) = \tilde{g}(\omega). \end{cases} \tag{22}$$

The newly developed filters $h_1, g_1, \tilde{h}_1$, and $\tilde{g}_1$ also construct the biorthogonal dual pair for perfect reconstruction if we choose

$$\begin{cases} p(2k) = 2h(2k) \\ p(2k+1) = 0. \end{cases} \tag{23}$$

Our lifting design is shown as Fig. 4, P_0 is the interpolating prediction process, and P_1 the updating filter, makes the down-

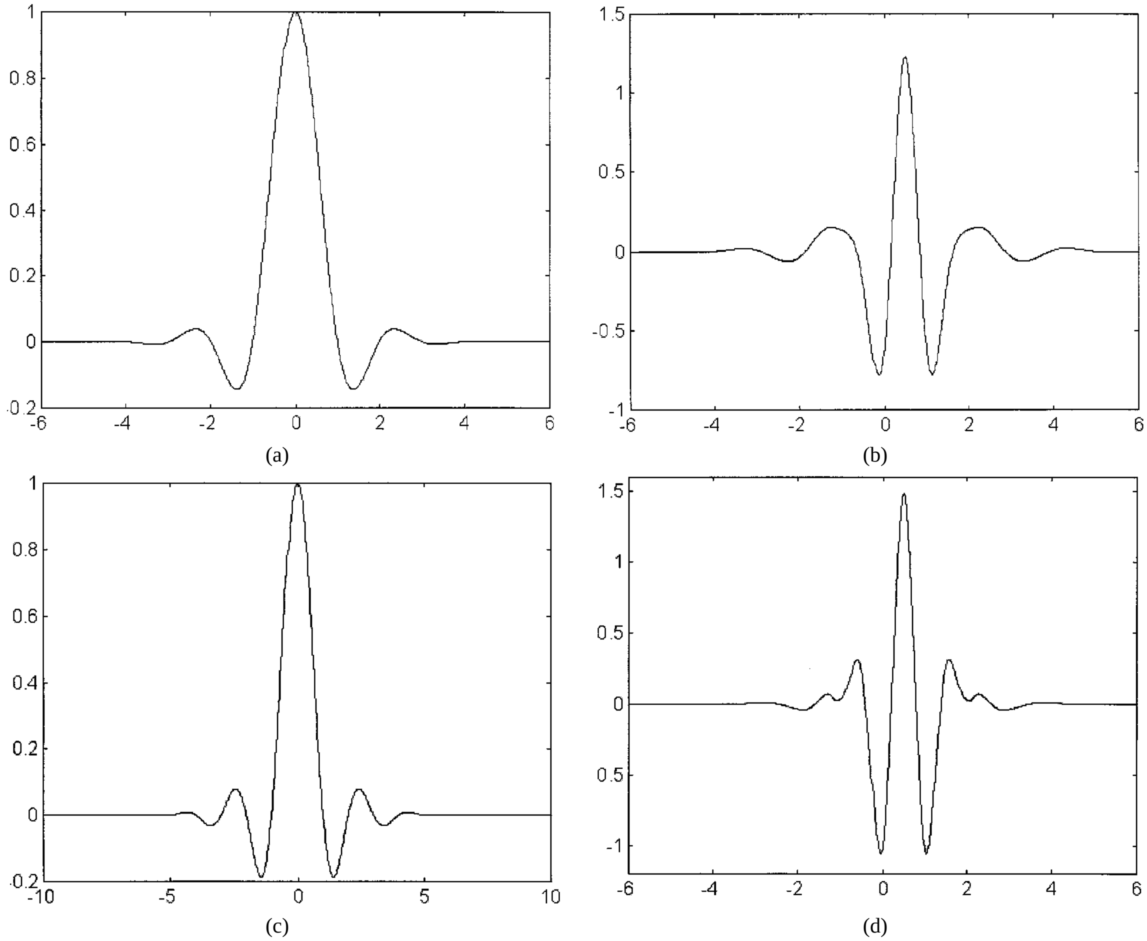

Fig. 7. Lagrange wavelets with $D = 9$. (a) Scaling, (b) wavelet, (c) dual scaling, and (d) dual wavelet.

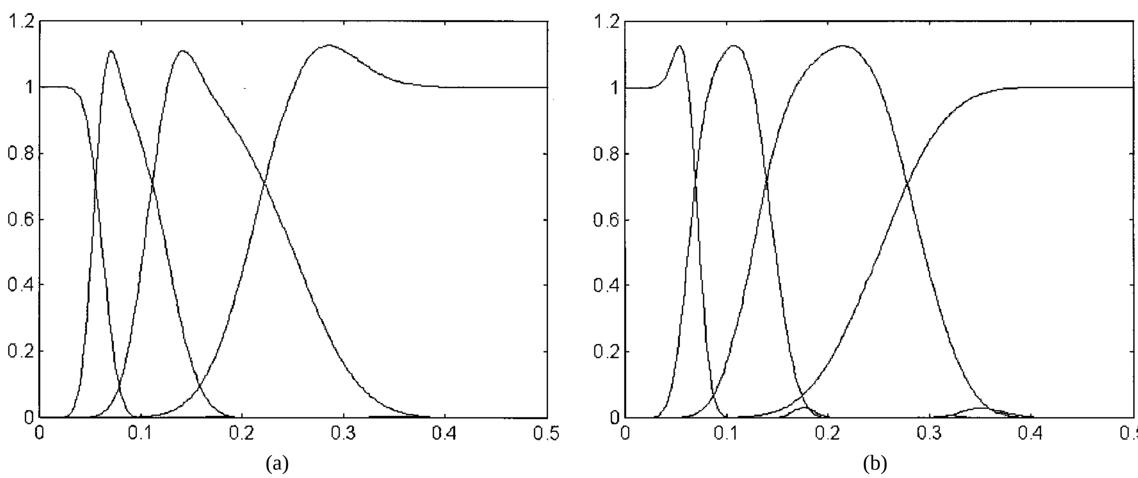

Fig. 8. Frequency response of equivalent filters ($D = 9$, $J = 3$). (a) Decomposition and (b) reconstruction.

sampling low-pass coefficients smoother. A simple example is to choose the impulse response of P_0 as

$$p_0(k) = 2h(2k - 1) \tag{24}$$

and the impulse response of P_1 as

$$p_1(k) = h(2k + 1). \tag{25}$$

In this case, the filter values of P_0 are 2 times larger than P_1, and the phase difference is 2 [i.e., $p_1(k) = (1/2)P_0(k + 1)$].

We emphasize that we use $\tilde{h}_1$ and $\tilde{g}_1$ as the analysis filterbanks, and h_1, g_1 as the reconstruction filterbanks. This may decrease reconstructed undulations of the coefficient error [because the coefficient error is like a small prime wavelet (with higher regularity), which is closely related to h_1, g_1]. Examples of biorthogonal lifting wavelets (with different regularity) generated by this scheme, and the associated equivalent subband filter responses are shown in Figs. 5–8.

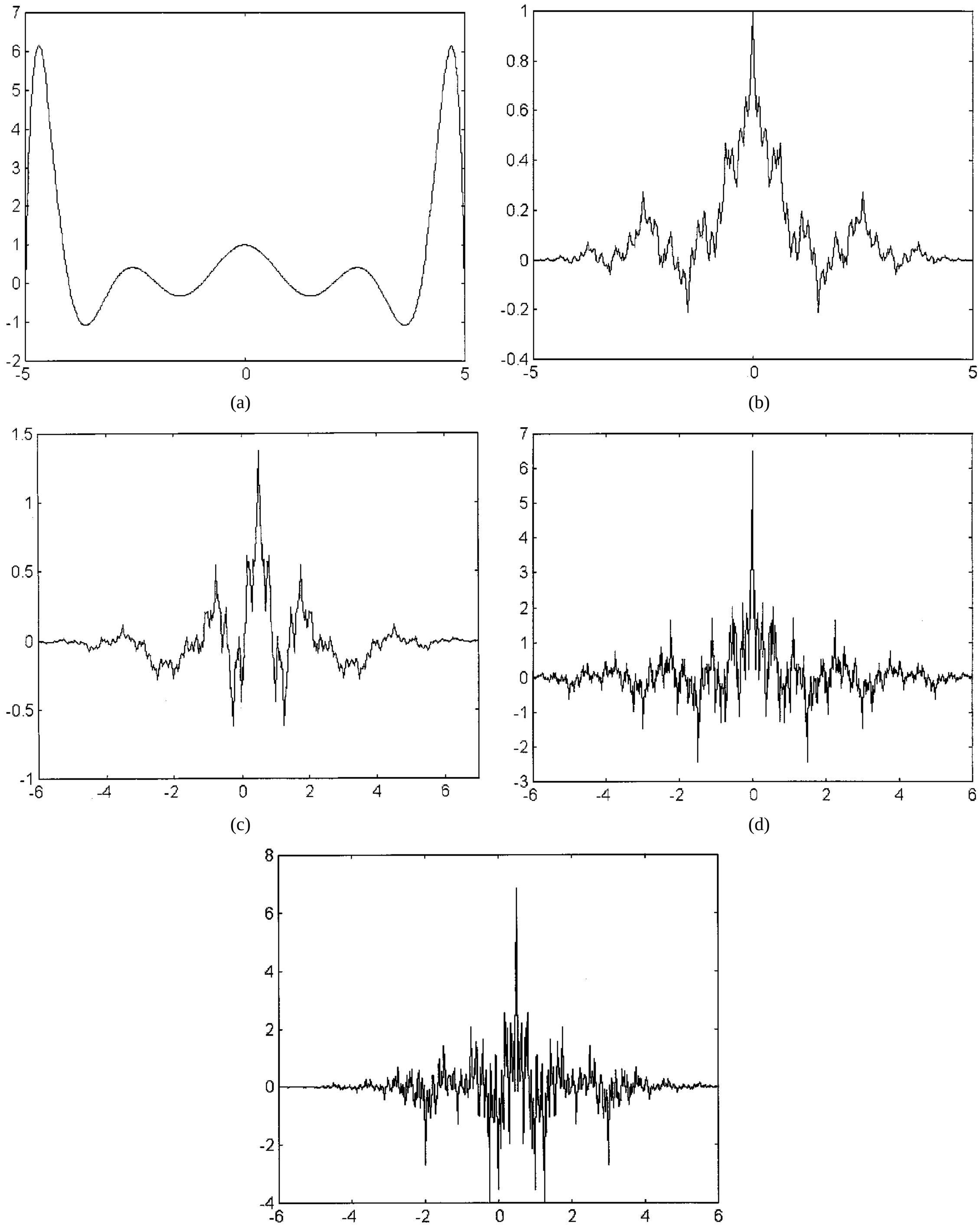

Fig. 9. Nonregularized Lagrange wavelets ($M = 5$). (a) Lagrange polynomial, (b) scaling, (c) wavelet, (d) dual scaling, and (e) dual wavelet.

B. Spline Lagrange Wavelets

Lagrange polynomials are natural interpolating expressions. By utilizing different expressions for the Lagrange polynomials, we construct extensions of interpolating wavelets. We define a class of symmetric Lagrange interpolating functional shells as

$$P_M(x) = \prod_{i=-M,\, i\neq 0}^{M} \frac{x-i}{-i} \tag{26}$$

and it is easy to verify that this Lagrange shell also satisfies the interpolating condition on discrete integer points, since

$$P_M(k) = \begin{cases} 1, & k = 0 \\ 0, & \text{otherwise.} \end{cases} \tag{27}$$

However, simply defining the filter response as

$$h(k) = \frac{1}{2} P\left(\frac{k}{2}\right), \qquad k = -M, M \tag{28}$$

leads to nonstable interpolating wavelets, as shown in Fig. 9.

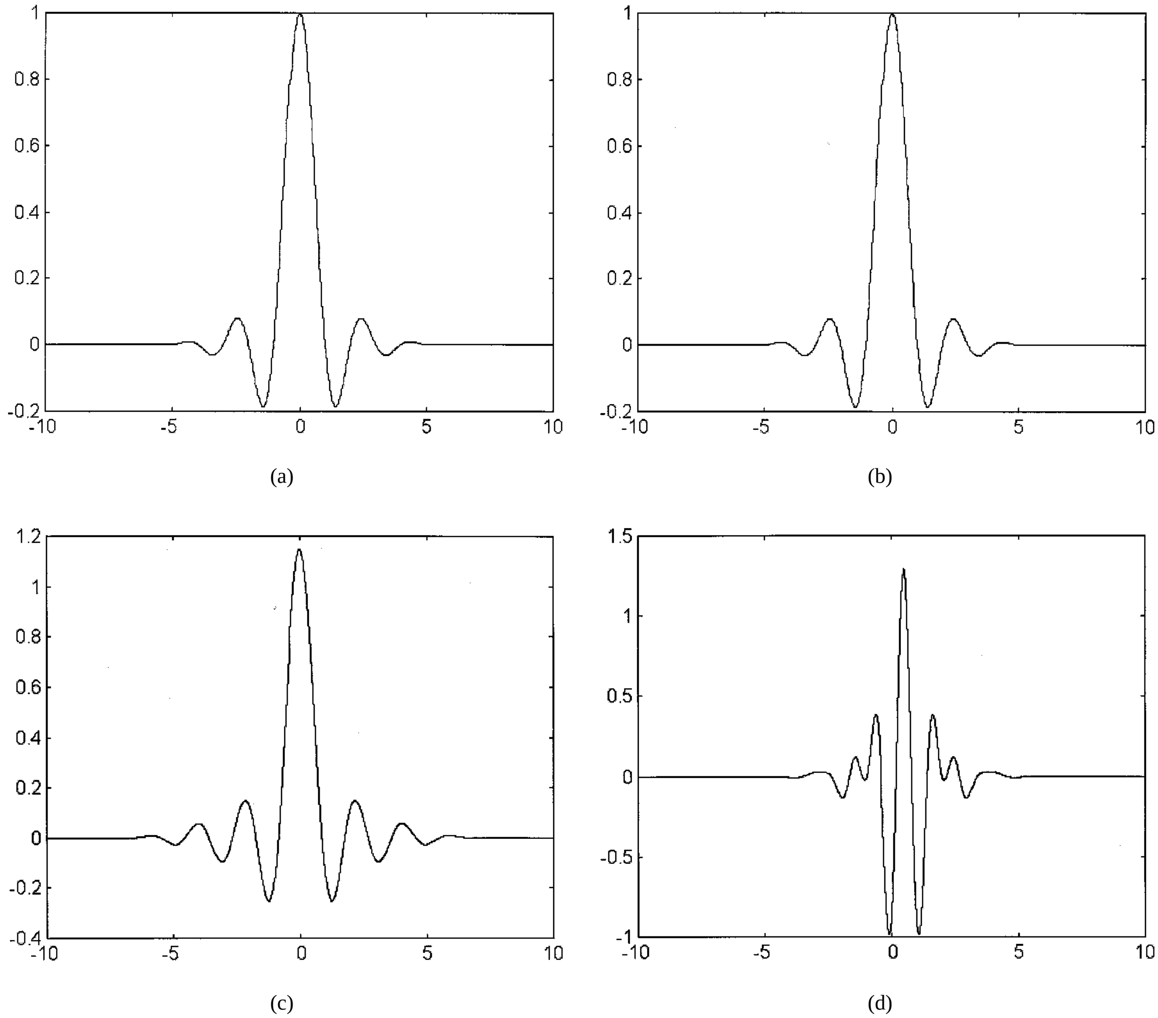

Fig. 10. B-Spline Lagrange DAF wavelets ($D = 4$, $\tau = 2$). (a) Scaling, (b) wavelet, (c) dual scaling, and (d) dual wavelet.

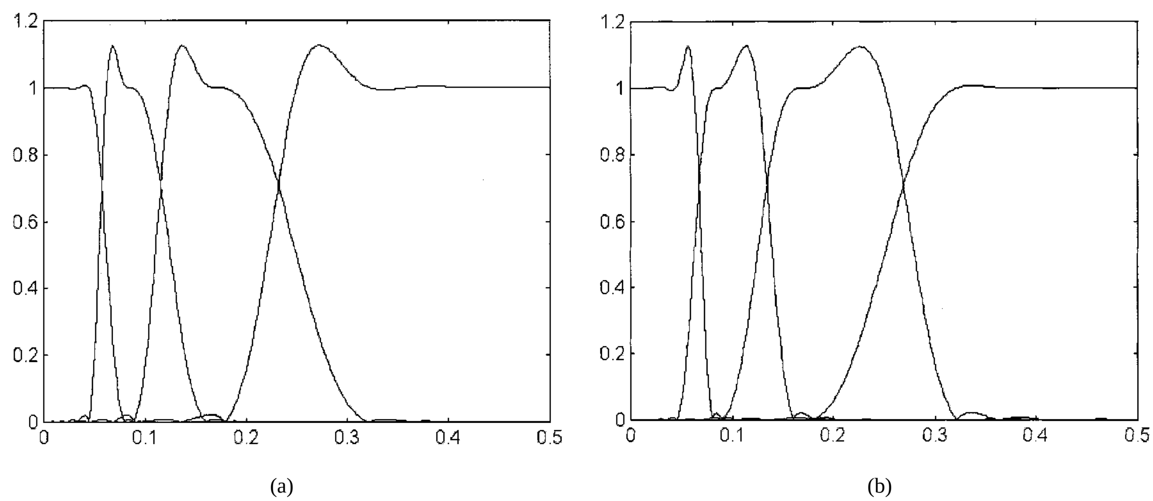

Fig. 11. Frequency response of equivalent filters ($D = 4$, $\tau = 2$). (a) Decomposition and (b) reconstruction.

Utilizing a smooth window, which vanishes at the zeros of the Lagrange polynomial, leads to more regular interpolating wavelets and equivalent subband filters (as in Figs. 10 and 11). If we select a well-defined B-spline function as the weight window, then the scaling function (mother wavelet) becomes an interpolating B-Spline Lagrange function (BSLF), given by

$$\phi_{M,\tau}(x) = \frac{\beta_D(x/\tau)}{\beta_D(0)} P_M(x) = \frac{\beta_D(x/\tau)}{\beta_D(0)} \prod_{i=-M,\, i\neq 0}^{M} \frac{x-i}{-i} \tag{29}$$

where D is the B-spline order, and τ is the scaling factor to control the window width. To ensure coincidence of the zeroes of the B-spline and the Lagrange polynomial, we set

$$2M = (D+1)\tau. \tag{30}$$

To preserve the interpolation condition, the B-spline envelope factor M should be an odd number. It is easy to show that when the B-spline order is $D = 4k+1$, τ can be any odd integer $(2k+1)$. If D is an even integer, then τ can only be 2. When $D = 4k-1$, we cannot construct an ideal interpolating shell according to the above definition. From the interpolation and self-induced scaling of the interpolating wavelets, it is easy to determine the subband filter response

$$h(k) = \frac{1}{2}\phi_M\left(\frac{k}{2}\right), \qquad k = -M, M. \tag{31}$$

C. Gaussian–Lagrange DAF Wavelets

The Gaussian Lagrange distributed approximating functional (GLDAF) can also be used as a basic scaling function to construct interpolating wavelets. These are

$$\phi_{M,\sigma}(x) = W_\sigma(x) P_M(x) = W_\sigma(x) \prod_{i=-M,\, i\neq 0}^{M} \frac{x-i}{-i} \tag{32}$$

where the B-spline window function is replaced by a Gaussian, $W_\sigma(x)$

$$W_\sigma(x) = e^{-x^2/2\sigma^2} \tag{33}$$

which satisfies the minimum frame bound condition in quantum physics. Here σ is a window-width parameter, and $P_M(x)$ is the Lagrange interpolation kernel. The DAF scaling function has been successfully utilized as the basis for an efficient and powerful grid method for quantum dynamical propagation [45]. Using the lifting scheme, a wavelet basis is generated. The Gaussian window in our DAF-wavelets efficiently smoothes out the Gibbs oscillations, which plague most conventional wavelet bases. The following equation shows the close connection between the B-spline and the Gaussian windows [39]:

$$\beta_D(x) \cong \sqrt{\frac{6}{\pi(D+1)}} \exp\left(\frac{-6x^2}{D+1}\right) \tag{34}$$

for large D. As in Fig. 12, if we choose the window width to be

$$\sigma = \tau\sqrt{(D+1)/12} \tag{35}$$

the Gaussian Lagrange (Lagrange DAF) wavelets are similar to the B-spline Lagrange wavelets. Usually, the Gaussian Lagrange DAF based wavelets are smoother and decay more rapidly than B-spline Lagrange wavelets as shown in Fig. 12. If we select more sophisticated window shapes, the Lagrange wavelets can be generalized further. We shall call these extensions Bell-windowed Lagrange wavelets. The above-mentioned interpolating wavelet construction using the Lagrange polynomials can be extended to produce arbitrary customer-designed wavelets using any continuous smooth functionals. The details will be presented in subsequent papers.

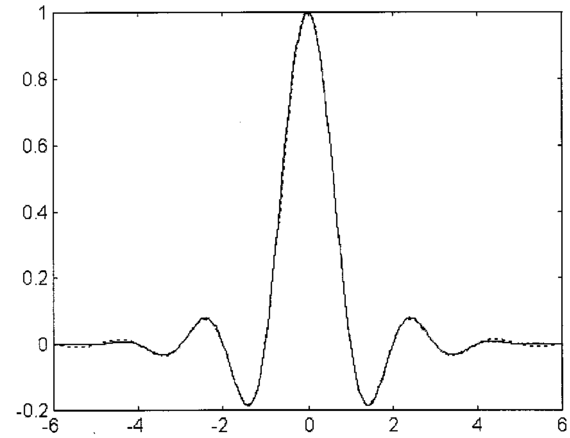

Fig. 12. Mother wavelet comparison ($D = 4$, $\tau = 2$). Solid: B-spline Lagrange and dotted: Gaussian Lagrange.

IV. VISUAL GROUP NORMALIZATION

It is well known that the mathematical theory of wavelet transforms and associated multiresolution analyses has applications in signal processing and engineering problems, where appropriate subband filters are the central entities. The goal of wavelet signal filtering is to preserve meaningful signal components, while efficiently reducing noise components. To this end, we shall previously developed magnitude normalization techniques [31], [32] and develop a new perceptual normalization to account for the human vision response.

From a signal processing point of view, wavelet coefficients can be regarded as results of the signal passing through an *equivalent decomposition filter* (EDF). The responses of the EDF $LC_{j,m}(\omega)$ are the combination of several recurrent subband filters at different stages. As shown in Fig. 6, the EDF amplitudes of different frequency subbands are different. Thus the magnitude of the decomposition coefficients in each of the subblocks will not exactly reproduce the true strength of the signal components. Stated differently, various EDFs are incompatible with each other in the wavelet transform. To adjust the magnitude of the response in each block, the decomposition coefficients are rescaled with respect to a common magnitude standard. Thus the EDF coefficients $C_{j,m}(k)$ on layer j and block m should be multiplied by a magnitude normalizing factor, $\lambda_{j,m}$, to obtain an adjusted magnitude representation. This factor is chosen as the reciprocal of the maximum magnitude of the frequency response of the equivalent filter on node (j,m)

$$\lambda_{j,m} = \frac{1}{\sup_{\omega\in\Omega}\{|LC_{j,m}(\omega)|\}} \qquad \Omega = [0, 2\pi]. \tag{36}$$

This idea was recently extended to *group normalization* (GN) of wavelet packets for signal processing [31], [32].

An image can be regarded as the result of a real object processed by a human visual system. The latter essentially has many subband filters. The responses of these human filters to various frequency distributions are not at all uniform. Therefore, an appropriate alteration of the wavelet coefficients is necessary. Actually, the human visual system is adaptive and has variable lenses and focuses for different visual environments. Using a just-noticeable distortion profile, we can efficiently remove the visual redundancy from decomposition coefficients and normalize them with respect to a standard of perceptual importance. A practical, simple model for perception efficiency has been presented by Watson, *et al.* [44] for data compression. This model is adapted here to construct the "perceptual lossless" response magnitude $Y_{j,m}$ for normalizing according to the visual response function

$$Y_{j,\,m} = a10^{k(\log(2^j f_0 d_m/R))^2} \tag{37}$$

where a defines the minimum detection threshold (the minimum possible $Y_{j,m}$ value). The $Y_{j,m}$ define a "perceptual lossless" quantization threshold. If the quantization factor is larger than $Y_{j,m}$, the reconstructed aliasing will be noticed by human eyes. An experimentally measured value of a is 0.495 for grayscale images [44]. The parameter k is an experimental constant chosen to ensure that the measured result match the mathematical model (33); it was taken to be 0.466 in [44]. R is the display visual resolution (DVR), which was defined in pixels/degree as

$$R \approx rv/57.3. \tag{38}$$

The viewing distance v (from eye to display) is given in centimeters (cm) and the display resolution r is given in pixels/cm (display or printer resolution). The term "direction" is introduced to identify the four possible combinations of low-pass and high-pass filtering (similar to the terminology LL, LH, HL, and HH in other wavelet references). The factor d_m is the directional response, which adjusts the minimum threshold by an amount that is a function of "direction." f_0 is the spatial frequency factor, which is used to adjust the spatial frequency for providing a reasonable fit to the experimental models. The spatial frequency is defined as

$$f \approx 2^{-j} R \tag{39}$$

where j is the layer of discrete wavelet decomposition and R is the display visual resolution [44]. Then $Y_{j,m}$, together with the magnitude normalizing factor $\lambda_{j,m}$, allows the creation of the perceptual lossless quantization matrix as

$$Q_{j,m} = 2Y_{j,m}\lambda_{j,m}. \tag{40}$$

This treatment provides a relatively simple, human-vision-based threshold technique for the restoration of the most important perceptual information in an image. We refer to the combination of the above mentioned two normalizations as the visual group normalization (VGN) of wavelet coefficients. Note here that we use λ_m for magnitude normalization and not for the wavelet "basis function amplitude" in [44], because the digital image decomposition is completely done using filter banks.

V. Softer Logic Masking Technique

Threshold masking techniques have been studied intensely in wavelet signal processing [4], [10], [19], [25], [32], [35]. Such maskings can be regarded as a bias-estimated *dead-zone limiter*. Jain [17] has shown that a nonlinear dead-zone limiter can improve the SNR for weak signal detection

$$\eta(y) = \operatorname{sgn}(y)(|y| - \delta)_+^\beta, \qquad -1 \le \beta \le 1 \tag{41}$$

where δ is a threshold value. The positive function $(x)_+$ is defined as

$$(x)_+ = \max\{x,\, 0\}. \tag{42}$$

Donoho has shown that the $\beta = 1$ case of the above expression is a nearly optimal estimator for adaptive NMR data smoothing and denoising [10].

The various threshold cutoffs of multiband expansion coefficients in hard logic masking methods are very similar to the cutoff of a FFT expansion. Thus, Gibbs oscillations like those associated with FFTs will also occur in a wavelet transform using a hard logic masking. Although hard logic masking methods with appropriate threshold values do not seriously change the magnitude of a signal after reconstruction, they can cause considerable edge distortions in a signal due to the interference of additional high frequency components induced by the cutoff. The higher the threshold value, the larger the Gibbs oscillation will be. Since image edges are especially important in visual perception, hard logic masking can only be used for weak-noise signal (or image) processing [such as electrocardiogram (ECG) signal filtering], where relatively small threshold values are required. In this paper, we propose a *softer logic masking* (SLM) method. In our SLM approach, a smooth transition band near each masking threshold is introduced so that any **decomposition coefficients which are smaller than the threshold value are** reduced gradually to zero, rather than being abruptly *set* to zero. This treatment efficiently suppresses the edge oscillations and preserves image edges, and consequently improves the resolution of the reconstructed image. The SLM method is implemented as

$$\hat{C}_{j,m}(k) = \operatorname{sgn}[C_{j,m}(k)] \times [|C_{j,m}(k)| - \delta]_+^\beta \times S\left[\overline{NC_{j,m}(k)}\right] \tag{43}$$

where $\hat{C}_{j,m}(k)$ denotes the decomposition coefficients to be retained in the reconstruction, and the quantity $\overline{NC_{j,m}(k)}$ is defined as

$$\overline{NC_{j,\,m}(k)} = \frac{|NC_{j,m}(k)|}{\max\limits_{(j,m)\in T}\{|NC_{j,m}(k)|\}}. \tag{44}$$

The softer logic window mapping, S: $[0,\,1] \to [0,\,1]$, is a nonlinear, monotonically increasing sigmoid functional. It is interesting to note that Nowak has also designed an alternative nonlinear technique independently to improve the Donoho

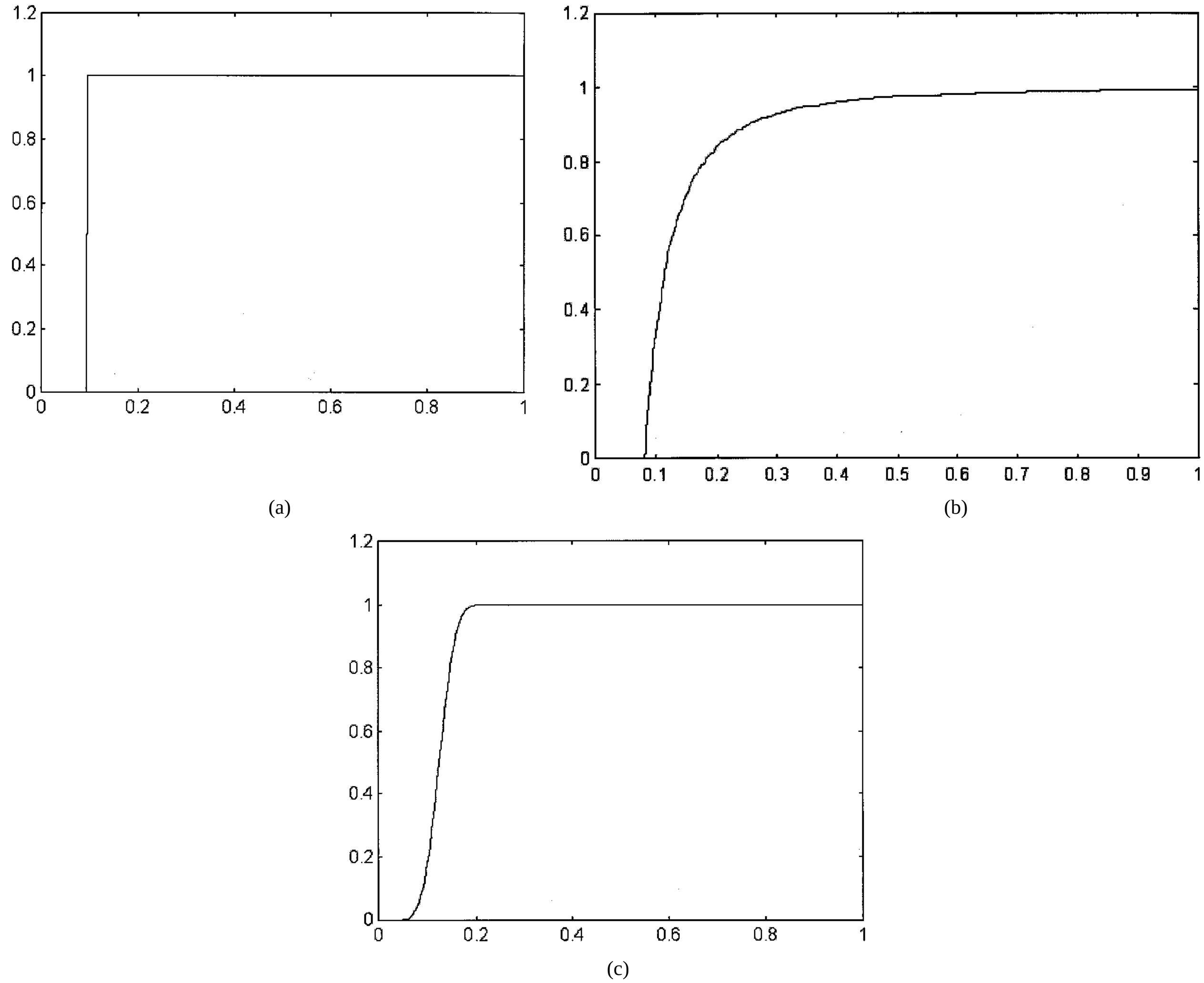

Fig. 13. Nonlinear masking windows. (a) Donoho window, (b) Nowak window, and (c) SLM window.

thresholding [25]. Nowak's nonlinear shrinkage functional has the form

$$\eta(y) = y\Lambda(y) \tag{45}$$

where the nonlinear window function Λ is defined as

$$\Lambda(y) = \left(\frac{y^2 - \delta^2}{y^2 + \dfrac{\delta^2}{N-1}} \right)_+ \tag{46}$$

and N is the signal size. A comparison of the hard logic, Nowak, and softer logic masking windows is depicted in Fig. 13. Our masking window is an infinitely smooth function in the region near threshold, with a maximum flat response both in the dead-zone and pass band. The Nowak window is smooth only to the right of the threshold, and has a less flat pass-band. Donoho's window is a nonsmooth signum function (no derivatives exist at threshold).

In two-dimensional (2-D) image processing, it is often important to preserve the image gradient along some xy-direction. For

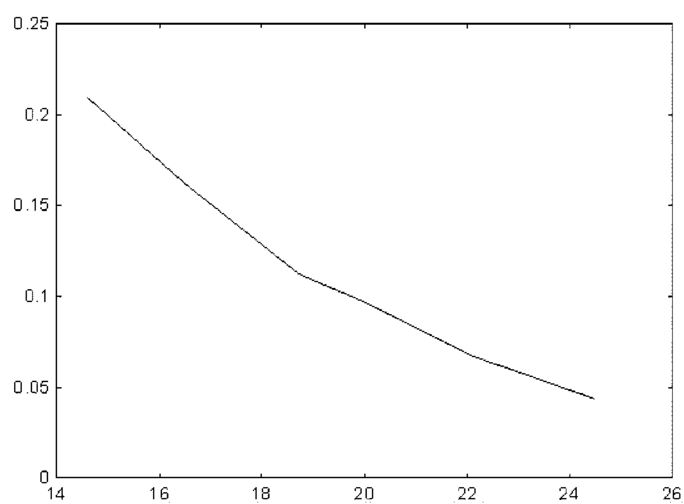

Fig. 14. Threshold rate based on noise PSNR level.

this purpose, we modify the aforementioned softer logic functional to

$$\hat{C}_{j,m}(k) = C_{j,m}(k) S \left(\frac{\overline{NC_{j,m}(k)} - \zeta}{1 - \zeta} \right) \tag{47}$$

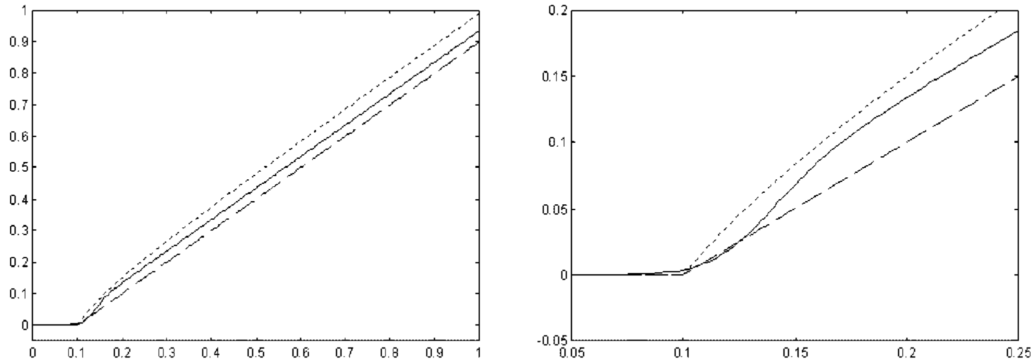

(a)

(b)

Fig. 15. Comparison of the nonlinear filtering. (a) Original and (b) enlargement around threshold area. (Dashed line: Donoho filter; dotted line: Nowak filter; and solid line: SLM filter.)

where ζ is a normalized adaptive threshold. The adjusted stretching factor $(1 - \zeta)$ is introduced to preserve the signal magnitude that is less contaminated by the noise. Johnstone and Silverman [19] provided a useful level-dependent method to estimate threshold ζ

$$\hat{\zeta}_j = \hat{\sigma}_j \sqrt{2 \log n} \tag{48}$$

where a robust estimation of the noise variance, σ_j^2, at each level can be obtained from the data as

$$\hat{\sigma}_j^2 = MAD \left\{ \overline{NC_{j,\,m}(k)} \right\} \Big/ 0.6745. \tag{49}$$

Here, we use $\overline{NC_{j,\,m}(k)}$ to replace the wavelet coefficients w_{jk} in [19], because our thresholding solution is based on normalized coefficients. "MAD" denotes the median absolute deviation from zero and the factor 0.6745 is chosen by calibration with the Gaussian distribution [19]. Choosing a threshold ζ_j to be proportional to $\sqrt{2 \log n}$ is done for the following reasons. If $Z_1, \ldots, Z_n$ are normally distributed random variables with mean zero and variance σ_j^2, then

$$\lim_{n \to \infty} P \left(\max_{1 \le i \le n} |Z_i / \sigma_i| > \sqrt{2 \log n} \right) = 0 \tag{50}$$

regardless of whether or not the variables are independent.

The noise model we assume for our illustrative example is white Gaussian. However, because we use the biorthogonal wavelet transform, the noise in the wavelet coefficients is not independent and identical distribution (iid) anymore (they are correlated now). The "conservative" properties of above equations come at the price of high threshold levels: in terms of PSNR loss in L^2 space, better performance is obtained with smaller thresholds [19]. A data-based threshold choice can then be obtained simply by minimizing the estimate with respect to threshold over the range $[0,\, \sigma\sqrt{2 \log n}]$.

In our earlier studies, we used a simplified variance approximation $\hat{\sigma}^2 = 1/1.35$, which assumed that the median is around 0.5 since the $\overline{NC_{j,\,m}(k)}$ have been normalized over [0, 1]. A more precise estimate can be obtained using the true median coefficient value that is image-independent. The variation of initial image PSNR vs. optimal uniform experimental threshold is shown in Fig. 14. Note that such a threshold curve is an average result of different images. When initial image PSNR is smaller (image is more contemned by noise), the uniform threshold will goes higher. Otherwise, the threshold will become lower. Actually, the best PSNR solution may depend on various image features (such as the texture, different spatial/orientation correlation, and spatial-frequency responses). It implies that the threshold is not only level (frequency) and orientation dependent, but also content (texture) dependent. Johnstone and Silverman's level dependent thresholding need to be extended to a block (spatial-frequency) and content dependent one to obtain the best PSNR results. Meanwhile, the best PSNR thresholds for different images (that share the same noise-corrupted level) are different. We will compare our simplified perceptual processing (VGN) and the level/block dependent, best PSNR thresholding in the section dealing with specific images.

The resulting nonlinear shrinkage filters η are compared in Fig. 15. As shown in the enlarged local area around the threshold, our softer logic masking shrinkage (the solid line in the middle) reflects the feature of smoothness around both ends. Recently, we have become aware that the SLM developed in our previous work to extract a target from formidable background noise [32] is quite similar to a method developed later, independently, by Chipman *et al.* [4].

VI. Experimental Results

Generally, the possible sources of image noise include photoelectric exchange, photo spots, errors in image communication, etc. The noise influences the visual perception to generate speckles, blips, ripples, bumps, ringings and aliasing. The noise distortion not only affects the visual quality of the images, but also degrades the efficiency of data compression and coding. Traditional image processing techniques can be classified as two kinds: linear or nonlinear. The principle methods of linear processing are local averaging, low-pass filtering, band-limit

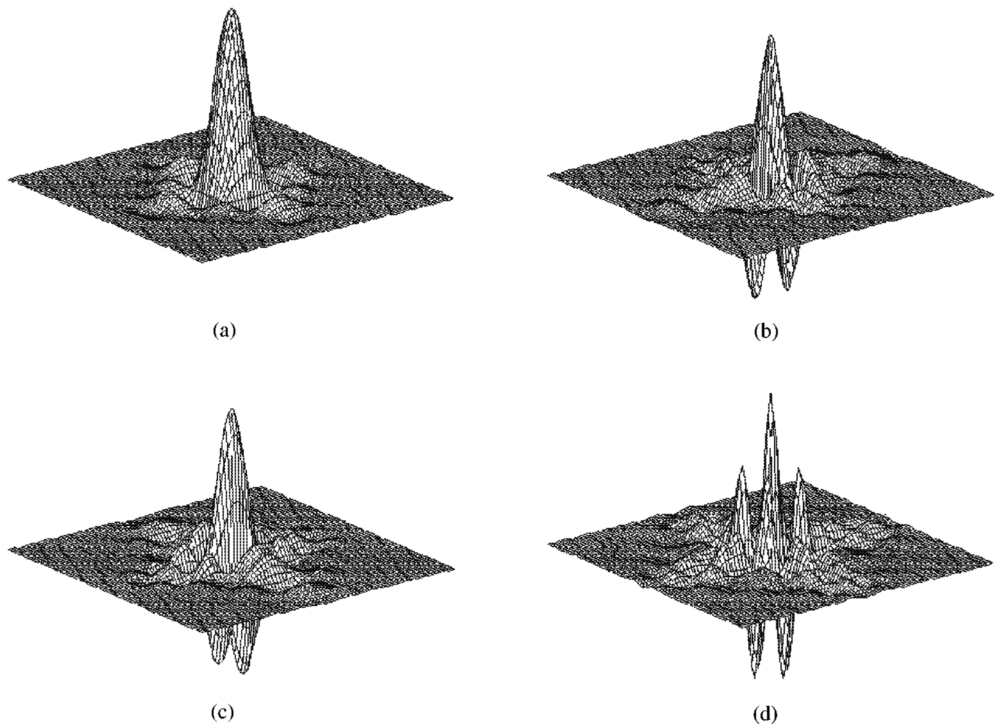

Fig. 16. Two-dimensional Gaussian Lagrange (LDAF) wavelets. (a) Scaling, (b) vertical, (c) horizontal, and (d) diagonal wavelets.

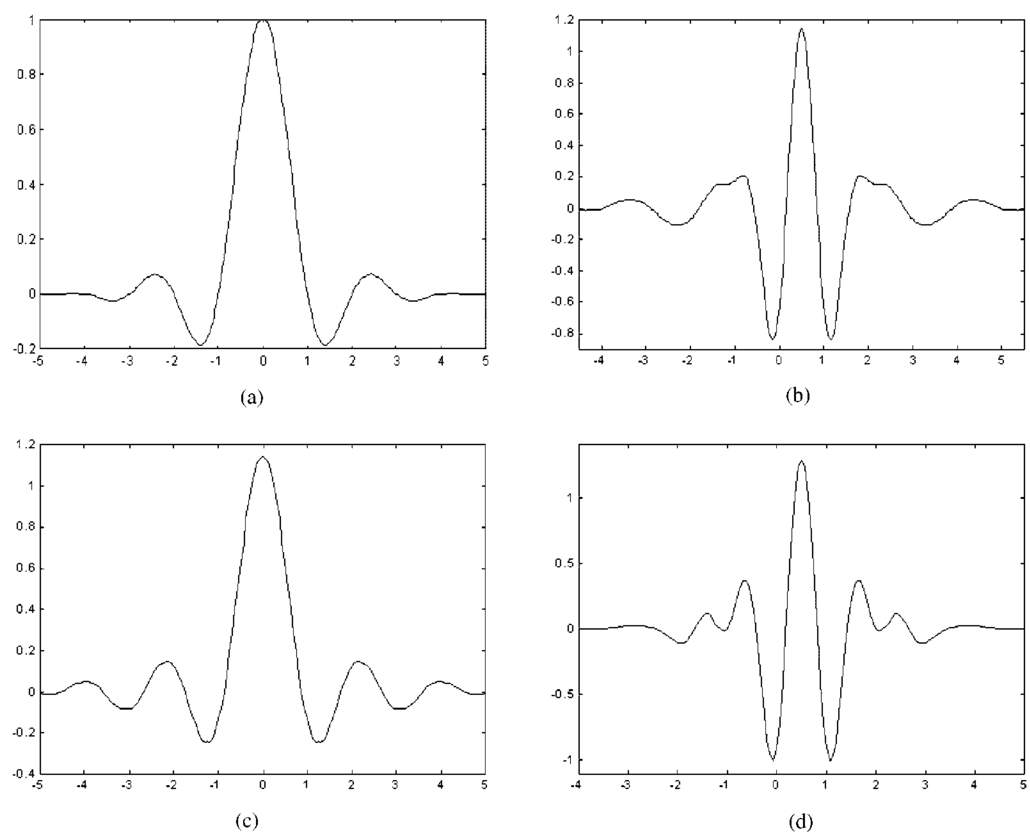

Fig. 17. Gaussian Lagrange (LDAF) wavelets. (a) Scaling, (b) wavelet, (c) dual scaling, and (d) dual wavelet.

filtering or multiframe averaging. Local averaging and low-pass filtering only preserve the low band frequency components of the image. The original pixel strength is substituted by an average of it with its neighboring pixels (within a square window).

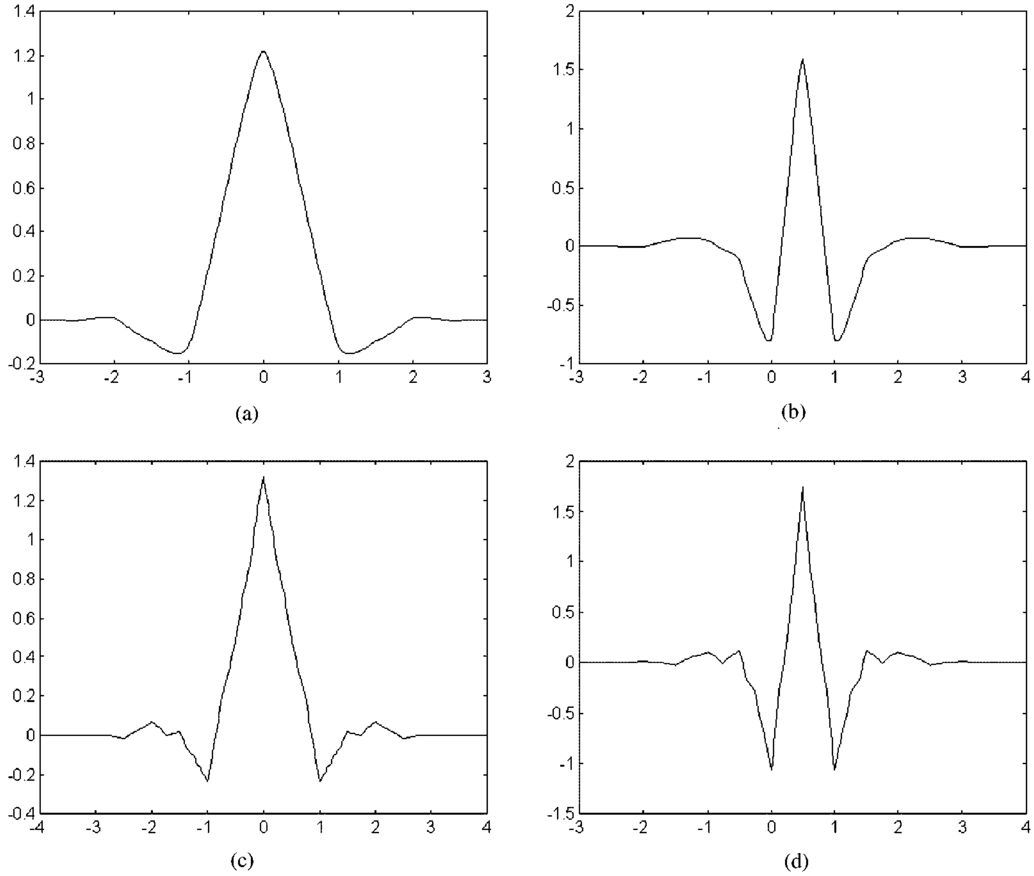

Fig. 18. B97 wavelets. (a) Scaling, (b) wavelet, (c) dual scaling, and (d) dual wavelet.

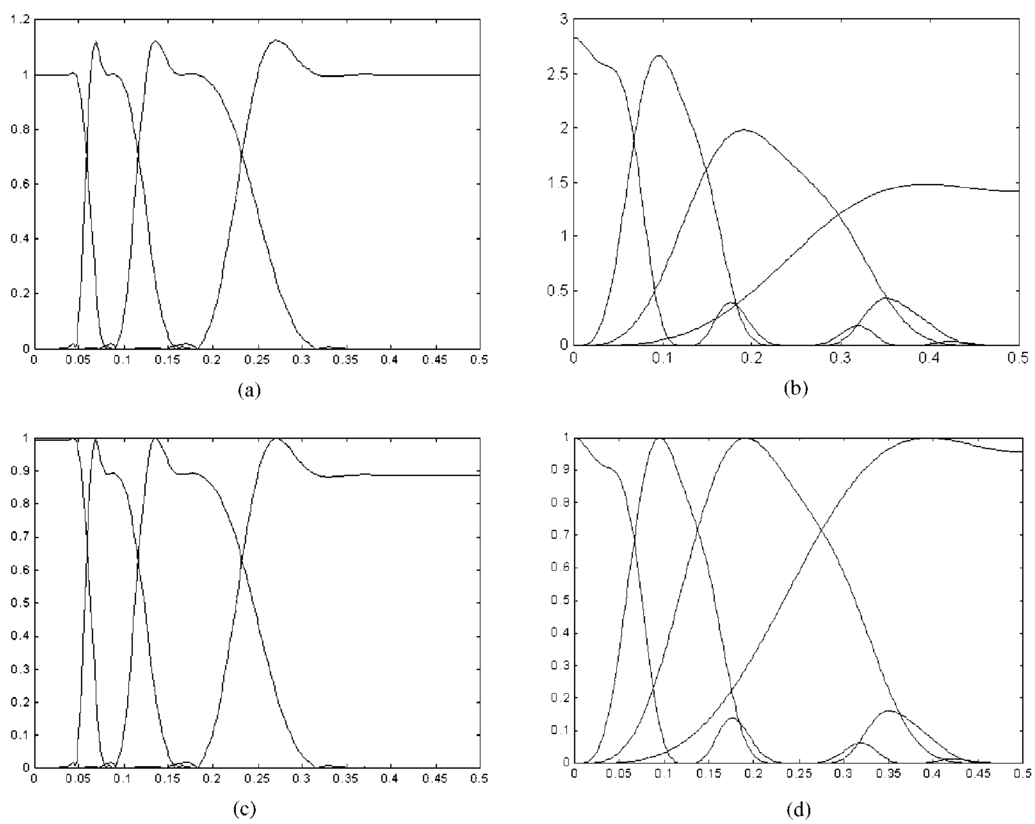

Fig. 19. Frequency response of equivalent filters. (a) Non-normalized response of Gaussian Lagrange (LDAF) wavelets, (b) non-normalized response of B97 wavelets, (c) normalized response of Gaussian Lagrange (LDAF) wavelets, and (d) normalized response of B97 wavelets.

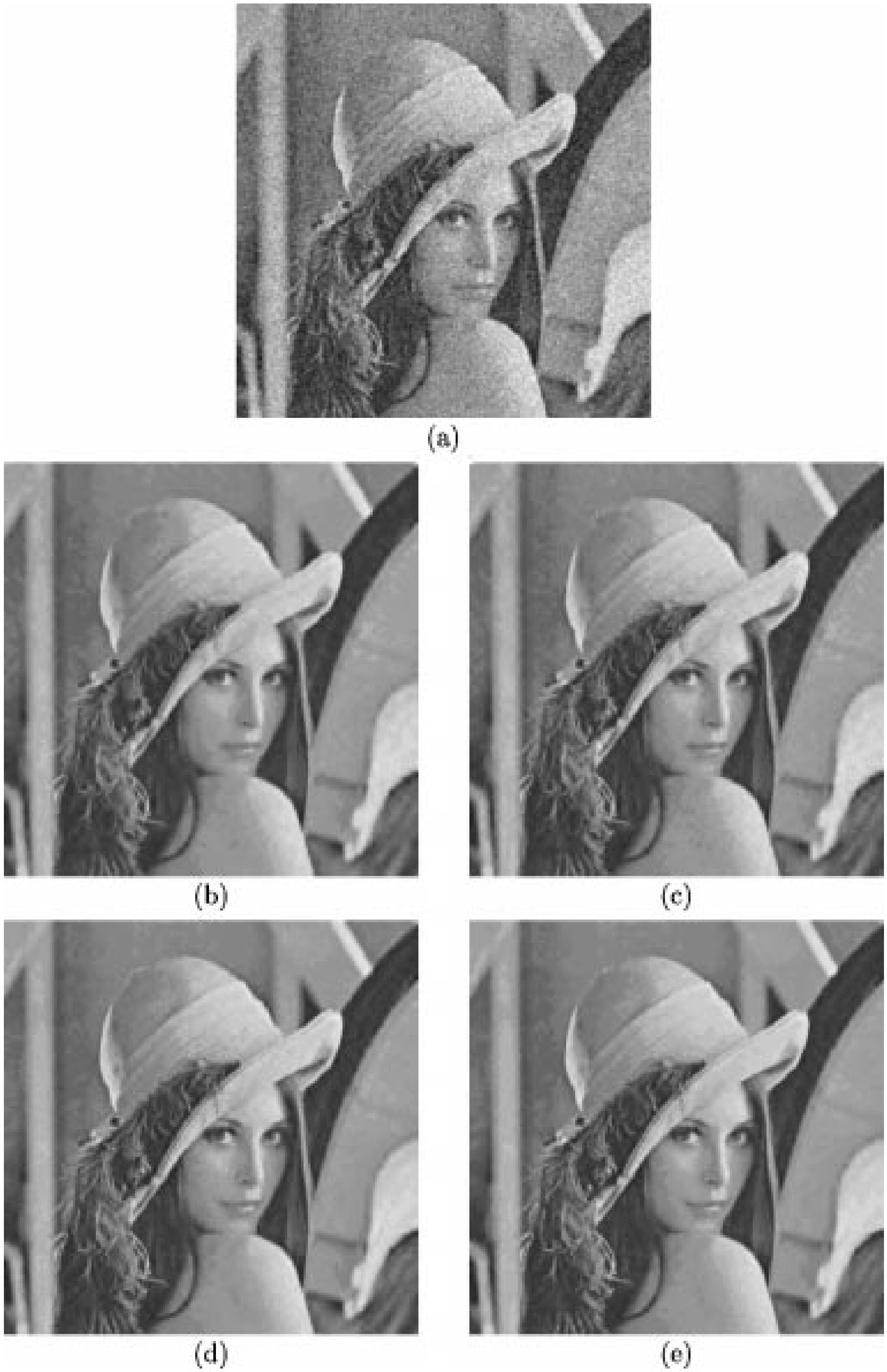

Fig. 20. VGN processing of Lena. (a) Noisy Lena (PSNR = 24.47 dB). (b) B97 VGN restoration (PSNR = 30.98 dB). (c) Halfband Lagrange wavelet VGN restoration. (PSNR = 30.87 dB). (d) B-spline Lagrange wavelet VGN restoration (PSNR = 31.38 dB). (e) Gaussian Lagrange (LDAF) wavelet VGN restoration (PSNR = 31.43 dB).

The mean error may be improved but the averaging process tends to blur the edges and finer details in the image. Band-limited filters are utilized to remove the regularly appearing dot matrix, texture and skew lines. They are useless for noise whose correlation is weak. Multiframe averaging requires that the images be still, and the noise distribution stationary. These con-

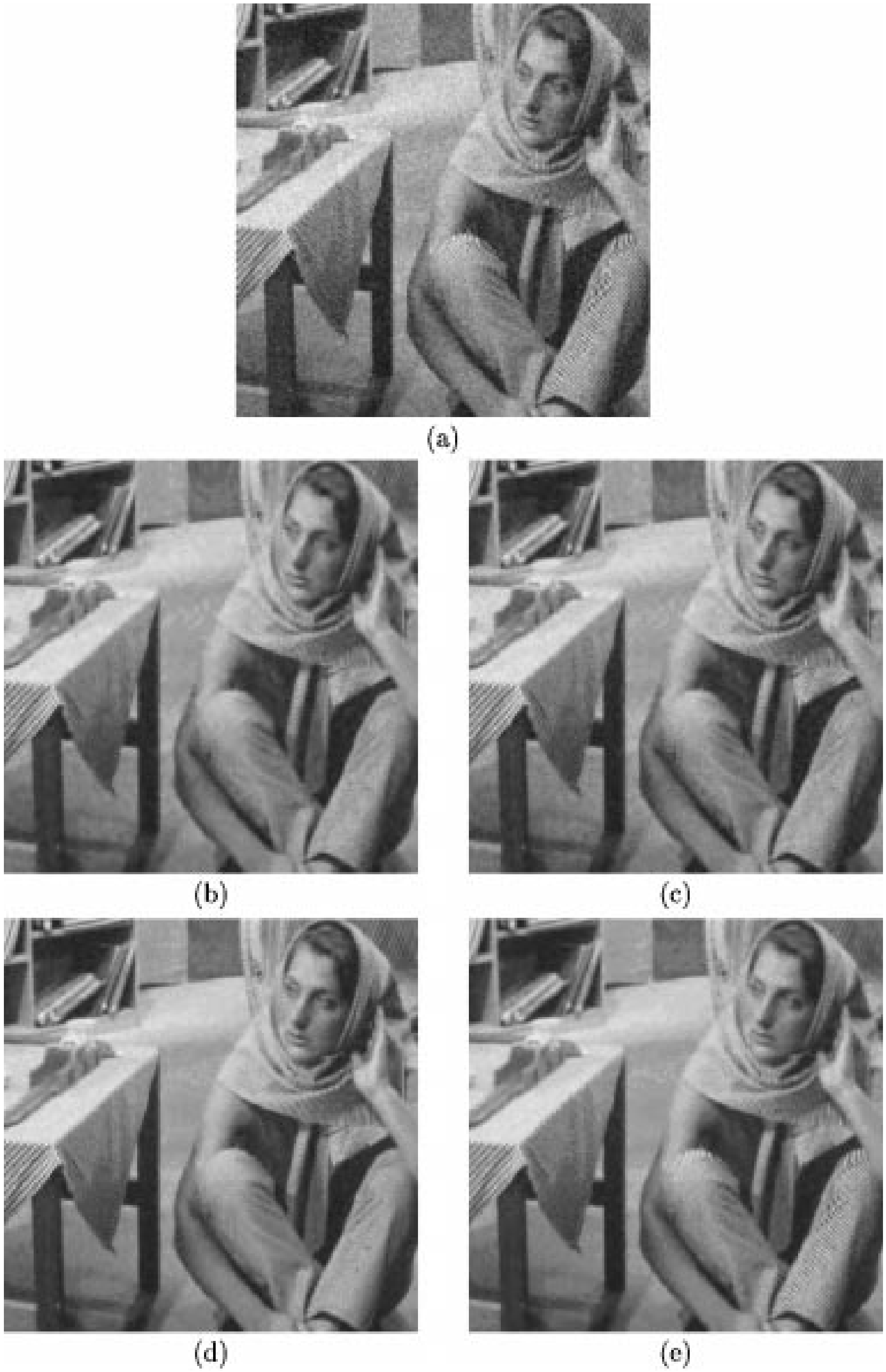

Fig. 21. VGN processing of Barbara. (a) Noisy Barbara (PSNR = 24.50 dB). (b) B97 VGN restoration (PSNR = 28.38 dB). (c) Halfband Lagrange wavelet VGN restoration. (PSNR = 28.13 dB). (d) B-spline Lagrange wavelet VGN restoration (PSNR = 28.97 dB). (d) Gaussian Lagrange (LDAF) VGN restoration (PSNR = 29.03 dB).

ditions are violated for motion picture images or for a space (time)-varying noisy background.

Traditionaly, image quality is characterized by a mean square error (*MSE*), which possesses the advantage of a simple mathematical structure. For a discrete signal $\{s(n)\}$ and its approximation $\{\hat{s}(n)\}$, $n = 0, \ldots, N$, the MSE is defined to be

$$MSE = \frac{1}{N} \sum_{n=0}^{N-1} [\hat{s}(n) - s(n)]^2. \tag{51}$$

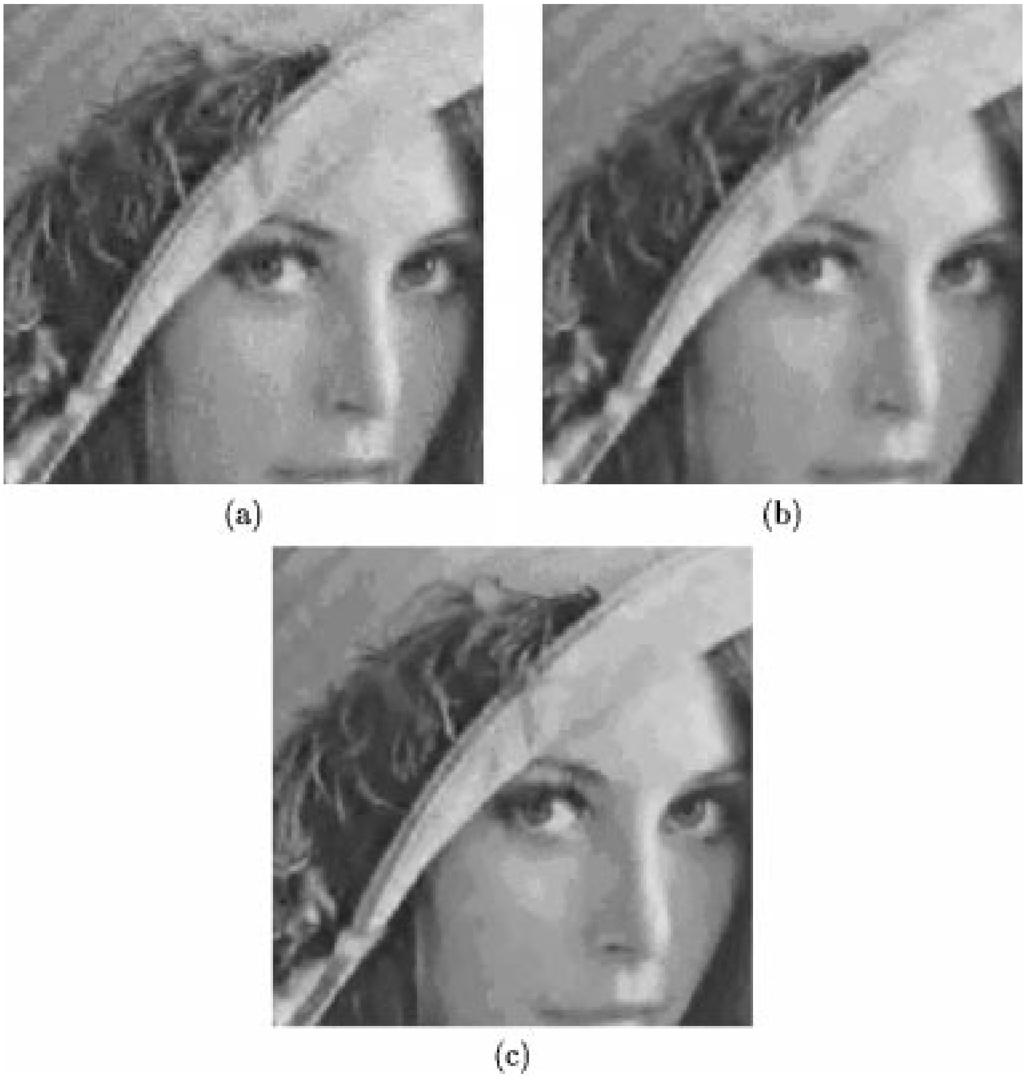

Fig. 22. Comparison of different masking methods on enlarged local area of Lena [all use the VGN technique, same Gaussian Lagrange (LDAF) wavelets as Figs. 20 and 21, PSNR is calculated using whole image but not local area]. (a) Donoho nonlinearity (PSNR $=$ 30.84 dB). (b) Nowak nonlinearity (PSNR $=$ 31.29 dB). (c) Our nonlinearity (PSNR $=$ 31.43 dB).

However, the *MSE* based evaluation standard, (such as $PSNR = \log[(255 \times 255)/MSE])$, can not exactly evaluate the image quality unless one neglects the effects of human perception. The minimum MSE rule causes strong undulations of the image level and destroys the smooth transition information around the pixels. Modified regularization methods may degrade the image resolution.

Generally, unsatisfactory traditional image processing is typically defined on the entire space (time) domain, which does not localize the space (time)-frequency details of the signal. Recent theoretical research shows that non-Gaussian and nonstationary characteristics are important components in human visual response [18], [38]. Human visual perception is more sensitive to image edges, which consist of sharp-changes of the neighboring luminance, because it is essentially adaptive and has variable lenses and focuses for different visual environments. To protect edge information as well as remove noise, modern image processing techniques are predominantly based on nonlinear methods. Before the smoothing process, the image edges, as well as perceptually sensitive texture must be detected.

TABLE I
PERFORMANCE COMPARISON BY PSNR (IN DECIBELS)

Noisy Images		Median	B97 (Non-VGN)	B97 (VGN)	GLDAF (VGN)
Barbara	17.60	22.01	22.81	24.27	24.63
	20.30	23.23	24.15	25.67	26.19
	24.50	24.39	27.01	28.38	29.03
Lena	16.46	26.23	23.38	26.74	27.30
	20.07	27.40	25.71	28.51	28.96
	24.47	28.41	28.18	30.98	31.43

The commonly used nonlinear filtering approaches include median filtering, and weighted averaging, etc. Median filtering uses the median value within the window instead of the original value of the pixel. This method causes less degradation for slanted functions or square functions, but suppresses those signal impulses which are shorter than half of the window length. This will degrade the image quality. **The most serious shortcomings of the weighted averaging method** are that the weighting-window is not adaptive, and large-scale, complicated calcula-

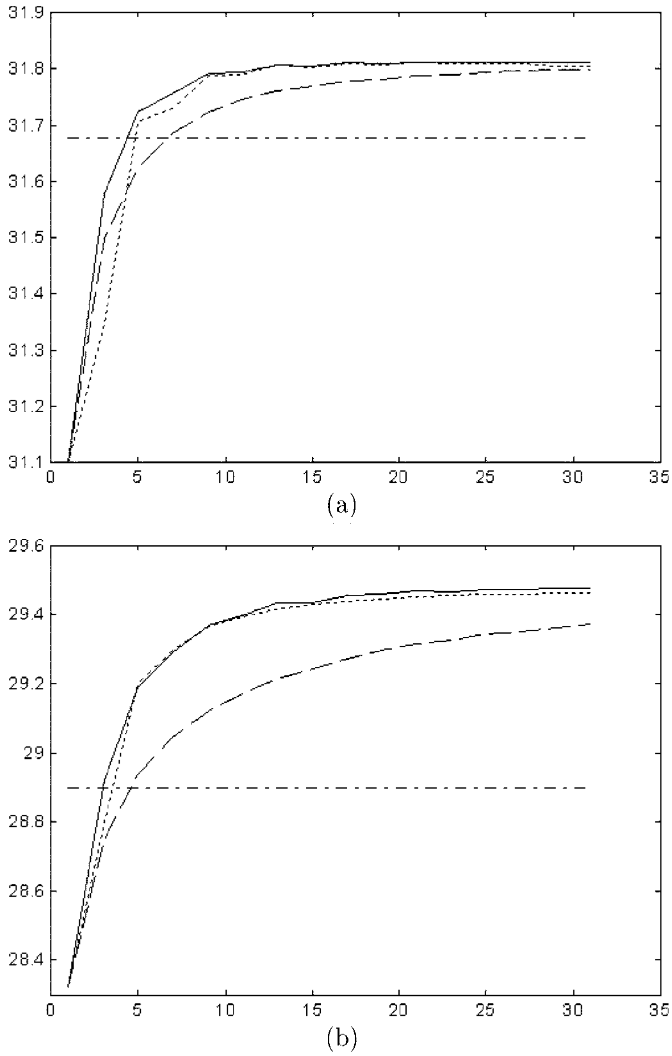

Fig. 23. Denoising performance comparison. [Solid line: Gaussian–Lagrange (LDAF) wavelet. Dotted line: B-spline Lagrange wavelet. Dashed: Half-band Lagrange wavelet. Dashed-dotted line: B97 wavelet.] (a) Denoising results for Lena. (b) Denoising results for Barbara.

TABLE II
DE-NOISING PSNR COMPARISON FOR LENA (PSNR = 24.6184 dB)

Filter Length = 2m + 1	De-noising PSNR Comparison for Lena (PSNR = 24.6184 dB)		
Order m	Half-band Lagrange	B-spline Lagrange	Gaussian Lagrange
1	31.1009	31.1009	31.1009
3	31.4958	31.3442	31.5760 (s = 1.25)
5	31.6231	31.7041	31.7220 (s = 1.70)
7	31.6848	31.7289	31.7549 (s = 1.97)
9	31.7215	31.7869	31.7901 (s = 2.35)
11	31.7445	31.7888	31.7926 (s = 2.55)
13	31.7591	31.8056	31.8073 (s = 2.93)
15	31.7693	31.8027	31.8042 (s = 3.04)
17	31.7763	31.8091	31.8112 (s = 3.39)
19	31.7816	31.8073	31.8084 (s = 3.45)
21	31.7859	31.8097	31.8112 (s = 3.73)
23	31.7895	31.8086	31.8097 (s = 3.78)
25	31.7925	31.8089	31.8107 (s = 3.96)
27	31.7950	31.8077	31.8099 (s = 4.04)
29	31.7973	31.8039	31.8102 (s = 4.14)
31	31.7992	31.8049	31.8102 (s = 4.25)

Notice: B97 (low-pass filter length = 9) wavelet de-noising PSNR = 31.6750 dB (Lena). We set factor h = 2 for B-spline Lagrange wavelets.

TABLE III
DE-NOISING PSNR COMPARISON FOR BARBARA (PSNR = 24.6394 dB)

Filter Length = 2m + 1	De-noising PSNR Comparison for Lena (PSNR = 24.6184 dB)		
Order m	Half-band Lagrange	B-spline Lagrange	Gaussian Lagrange
1	28.3236	28.3236	28.3236
3	28.7502	28.7993	28.9197 (s = 1.32)
5	28.9379	29.1999	29.1878 (s = 1.88)
7	29.0464	29.2964	29.2905 (s = 2.19)
9	29.1198	29.3663	29.3693 (s = 2.57)
11	29.1733	29.3931	29.3962 (s = 2.82)
13	29.2137	29.4173	29.4304 (s = 3.15)
15	29.2460	29.4277	29.4353 (s = 3.34)
17	29.2726	29.4390	29.4545 (s = 3.66)
19	29.2947	29.4449	29.4568 (s = 3.84)
21	29.3131	29.4511	29.4702 (s = 4.10)
23	29.3285	29.4544	29.4673 (s = 4.23)
25	29.3417	29.4584	29.4742 (s = 4.48)
27	29.3531	29.4611	29.4724 (s = 4.70)
29	29.3627	29.4640	29.4779 (s = 4.85)
31	29.3711	29.4651	29.4758 (s = 4.94)

Notice: B97 wavelet (low-pass filter length = 9) de-noising PSNR = 28.8978 dB (Barbara). We set factor h = 2 for B-spline Lagrange wavelets.

tions are required to generate pixel values. As the window is made wider, more details are removed.

The efficient HVS-based image processing techniques possess the advantages of

1) long range decorrelation for convenience of compression and filtering;
2) high perceptual sensitivity and robustness;
3) filtering according to human visual response.
4) it can be carried out with real-time processing.

It therefore can enhance the most important visual information, such as edges, while suppressing the flat regions and background.

The space (time)-scale logarithmic response characteristic of the wavelet transform is similar to the HVS response. Visual perception is sensitive to narrow band low-pass components, and is insensitive to wide band high frequency components. Moreover, from research in neurophysiology and psychophysical studies, the direction-selective cortex filtering is very much like a 2-D wavelet decomposition. The high-pass coefficients of the wavelet transform can be regarded as a visible difference predictor (VDP).

Utilizing the modified wavelet analysis-VGN wavelet transform presented in this paper, we correct the problem that the raw magnitudes of the transform coefficients do not exactly yield the perceptual strength of digital images. The nonlinear SLM filtering provides edge-preservation for images, which removes the haziness encountered with commonly used filtering techniques.

To test our approaches, benchmark 512×512 Y-component images are employed. The first test is for the so-called "Lena" image, which possesses clear sharp edges, strong contrast and brightness. The second picture tested is "Barbara." The variety of texture components and consequently high frequency edges in the Barbara image create considerable difficulties for commonly used filtering techniques. We focus on 2-D Gaussian Lagrange (Lagrange DAF) wavelets for image processing. The selected parameters are $M = 5$, and $\sigma = 1.73$. The SLM nonlinearity used in this paper is the same as (48). The four 2-D Gaussian Lagrange (Lagrange DAF) wavelets are shown in Fig. 16.

The popular B97 wavelets [7], [43] are used in comparison with the generalized Lagrange wavelet technique. As shown in Fig. 17, both Gaussian Lagrange (LDAF) wavelets and their dual partners display excellent smoothness and rapid decay compared with the B97 wavelets (Fig. 18). The Gaussian window efficiently smoothes out the fractal-like oscillations, which plague many wavelets. The EDF responses of both the DAF and B97 wavelets

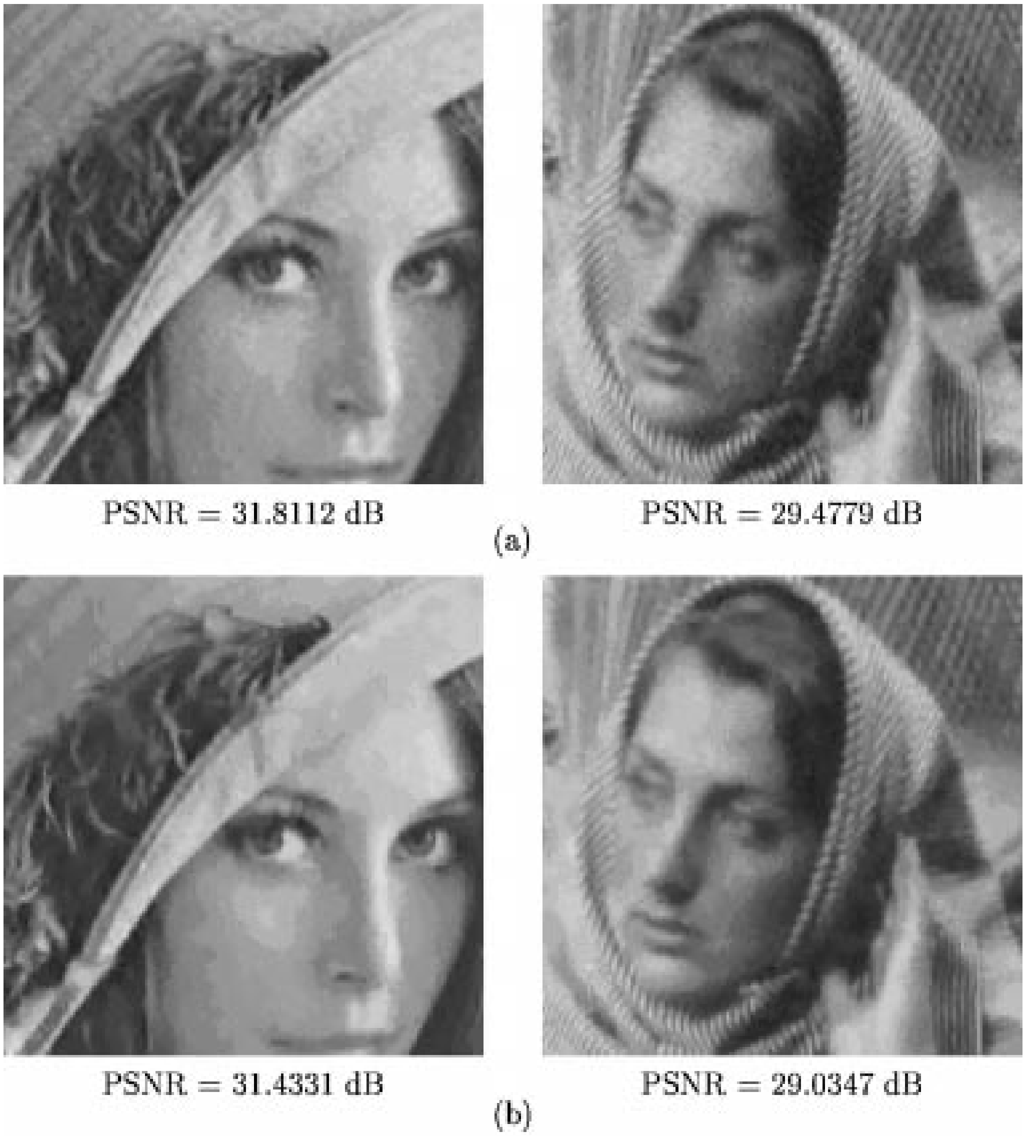

Fig. 24. Visual performance comparison. (a) Softer logic masking using block-dependent threshold (best PSNR). (b) Softer logic masking using VGN (lower PSNR).

are shown in Fig. 19. It is obvious that the DAFs possess smaller sidelobes, and therefore lead to less frequency leakage distortion.

In Figs. 20(a) and 21(a), respectively, we show the result of Gaussian white noise added to the original Lena and Barbara images. The PSNR results of median filtering, B97-wavelet filtering, B97-wavelet VGN filtering and GLDAF-wavelet VGN processing are compared in Table I, while the perceptual quality of the B97-wavelet VGN, half-band Lagrange wavelet VGN, B-spline Lagrange wavelet VGN, and Gaussian Lagrange (LDAF) wavelet VGN processed images (Lena and Barbara) are shown in Figs. 20(b)–(e) and 21(b)–(e), respectively. It is evident that our VGN wavelet technique yields better PSNR, contrast and edge-preservation results, as well as provides high quality visual performance. An additional performance comparison of different nonlinear maskings (Donoho, Nowak, and softer logic) is shown in Fig. 22.

Our image processing method can be regarded as a blind restoration technique for any image. If we assume the noise-free image is known, an image-dependent threshold choice using the threshold approximation in reference [19] can then be obtained simply by minimizing the estimate with respect to threshold over the range $[0, \sigma\sqrt{2\log n}]$ according to

$$\hat{\zeta}_{j,d} = \max_{j,d}\left\{PSNR\left(\hat{I}\left(\hat{\zeta}_{j,d}, I_{noise}\right), I\right)\right\} \tag{52}$$

where

- $\hat{\zeta}_{j,d}$ threshold estimate at decomposition layer j and spatial direction d (HL, LH or HH);
- I noise-free image;
- I_{noise} noise-corrupted image;
- $\hat{I}$ softer logic masking approximation of the image.

We emphasize here that the threshold is not only level dependent as in [19], but also spatial-direction-based (because of the 2-D decomposition). In VGN processing, we require the LH and HL orientations (horizontal and vertical) to possess the same human visual perceptual sensitivity (the threshold should be same). However, for a PSNR-based restoration, one violates the balance between these two orientations to obtain the best PSNR results.

In Tables II and III, the PSNR performance comparison of level-based denoising methods (all using the softer logic masking) show that Gaussian Lagrange (LDAF) wavelet provides the best PSNR results using different width factor and order choices. The B-spline Lagrange wavelet also yields excellent performance, with easier parameter selection (in the experiment, we only used the factor $\eta = 2$). For high polynomial order, half-band Lagrange wavelet is also superior to the popular B97 wavelet. A plot comparing PSNR is given in Fig. 23.

The visual quality comparison of the level-dependent threshold method [19] and VGN are shown in Fig. 24. Although the VGN method possess the smaller PSNR (0.4 dB less), the perceptual quality seems better.

VII. Conclusions

This paper discusses the design of interpolating wavelets based on Lagrange interpolating functions and their application in image processing. An attractive property of the resulting interpolating wavelets is that the wavelet multiresolution analysis is realized by discrete sampling. Thus pre- and post-conditioning are not needed for an accurate wavelet analysis. The wavelet coefficients are obtained from linear combinations of sample values rather than from integrals, which implies the possibility of using parallel computation techniques. Theoretically, our approach is closely related to the finite element technique for the numerical solution of partial differential equations, the subdivision scheme for interpolation approximations, multigrid methods and surface fitting techniques. In this paper, we generalize the definition of interpolating Lagrange wavelets and produce three different biorthogonal interpolating Lagrange wavelets, namely Halfband Lagrange wavelets, B-spline Lagrange wavelets and Gaussian–Lagrange (LDAF) wavelets.

Halfband Lagrange wavelets can be regarded as an extension of the Dubuc interpolating functionals, auto-correlation shell wavelet analysis and halfband filters. B-spline Lagrange wavelets and Gaussian Lagrange (LDAF) wavelets are generated by B-spline windowing and Gaussian windowing of a Lagrange functional, respectively, and lead to increased smoothness and localization compared to the basic Lagrange wavelets. *Lagrange distributed approximating functionals* (LDAF) are taken to be scaling functions (wavelet-DAFs). DAFs are smoothly decaying in both time and frequency representations. The present work extends the DAF approach to digital signal and image processing by constructing new biorthogonal wavelets using a lifting scheme.

For image processing applications, we combine two important techniques, the coefficient normalization method and perceptual lossless quantization based on *human vision systems* (HVS). The resulting combined technique is called *visual group normalization* (VGN) processing [31]. The concept of *visual lossless quantization* (VLQ) leads to a potential breakthrough compared to the traditional Shannon rate-distortion theory in perception-based information processing. A modified version of Donoho's soft thresholding for image restoration, termed the *softer logic masking* (SLM) technique, is introduced for dealing with extremely noisy backgrounds. This technique better preserves the important visual edges and contrast transition portions of an image and is readily adaptable to human vision. Computational results show that our generalized Lagrange and Lagrange-DAF wavelet based VGN processing is extremely efficient and robust for digital image blind restoration and yield good performance.

References

[1] R. Ansari, C. Guillemot, and J. F. Kaiser, "Wavelet construction using Lagrange halfband filters," *IEEE Trans. Circuits Syst.*, vol. 38, pp. 1116–1118, Sept. 1991.
[2] R. Baraniuk and D. Jones, "Signal-dependent time-frequency analysis using a radially Gaussian kernel," *Signal Process.*, vol. 32, pp. 263–284, 1993.
[3] C. M. Brislawn, "Preservation of subband symmetry in multirate signal coding," *IEEE Trans. Signal Processing*, vol. 43, pp. 3046–3050, Dec. 1995.
[4] H. A. Chipman, E. D. Kolaczyk, and R. E. McCulloch, "Adaptive Bayesian wavelet shrinkage," *J. Amer. Statist. Assoc.*, vol. 92, no. 440, pp. 1413–1421, Dec. 1997.
[5] C. K. Chui, *An Introduction to Wavelets*. New York: Academic, 1992.
[6] A. Cohen, "Biorthogonal wavelets," in *Wavelets: A Tutorial in Wavelet Theory and Applications*, C. K. Chui, Ed. New York: Academic, 1992, pp. 123–152.
[7] A. Cohen, I. Daubechies, and J. C. Feauveau, "Biorthogonal bases of compactly supported wavelets," *Commun. Pure Appl. Math*, vol. 45, pp. 485–560, 1992.
[8] I. Daubechies, "Orthonormal bases of compactly supported wavelets," *Commun. Pure Appl. Math.*, vol. 41, no. 11, pp. 909–996, 1988.
[9] G. Deslauriers and S. Dubuc, "Symmetric iterative interpolation processes," *Construct. Approx.*, vol. 5, pp. 49–68, 1989.
[10] D. L. Donoho, "De-noising by soft-threshold," *IEEE Trans. Inform. Theory*, vol. 41, no. 3, pp. 613–627, 1995.
[11] ——, "Interpolating wavelet transform," Stanford Univ., Stanford, CA, 1992, to be published.
[12] S. Dubuc, "Interpolation through an iterative scheme," *J. Math. Anal. Applicat.*, vol. 114, pp. 185–204, 1986.
[13] A. Harten, "Multiresolution representation of data: A general framework," *SIAM J. Numer. Anal.*, vol. 33, no. 3, pp. 1205–1256, 1996.
[14] C. Herley and M. Vetterli, "Orthogonal time-varying filter banks and wavelet packets," *IEEE Trans. Signal Processing*, vol. 42, pp. 2650–2663, Oct. 1994.
[15] C. Herley, Z. Xiong, K. Ramchandran, and M. T. Orchard, "Joint space-frequency segmentation using balanced wavelet packets trees for least-cost image representation," *IEEE Trans. Image Processing*, vol. 6, pp. 1213–1230, Sept. 1997.
[16] D. K. Hoffman, N. Nayar, O. A. Sharafeddin, and D. J. Kouri, "Analytic banded approximation for the discretized free propagator," *J. Phys. Chem.*, vol. 95, no. 21, pp. 8299–8305, 1991.
[17] L. C. Jain, N. M. Blachman, and P. M. Chapell, "Interference suppression by biased nonlinearities," *IEEE Trans. Inform. Technol.*, vol. 41, no. 2, pp. 496–507, 1995.
[18] N. Jayant, J. Johnston, and R. Safranek, "Signal compression based on models of human perception," *Proc. IEEE*, vol. 81, pp. 1385–1422, Oct. 1993.
[19] I. M. Johnstone and B. W. Silverman, "Wavelet threshold estimators for data with correlated noise," *J. R. Statist. Soc. B*, vol. 59, pp. 319–351, 1997.
[20] J. Kovacevic and M. Vetterli, "Perfect reconstruction filter banks with rational sampling factors," *IEEE Trans. Signal Processing*, vol. 41, pp. 2047–2066, June 1993.
[21] J. Kovacevic and W. Swelden, "Wavelet families of increasing order in arbitrary dimensions," *IEEE Trans. Image Processing*, vol. 9, pp. 480–496, Mar. 2000.
[22] A. F. Laine, S. Schuler, J. Fan, and W. Huda, "Mammographic feature enhancement by multiscale analysis," *IEEE Trans. Med. Imag.*, vol. 13, pp. 725–740, 1994.
[23] S. Mallat, "A theory for multiresolution signal decomposition: The wavelet representation," *IEEE Trans. Pattern Anal. Machine Intell.*, vol. 11, pp. 674–693, July 1989.
[24] Y. Meyer, *Wavelets Algorithms and Applications*. Philadelphia, PA: SIAM, 1993.
[25] R. Nowak, D. Nowak, R. Baraniuk, and R. Hellman, "Wavelet domain filtering for nuclear medicine imaging," in *Proc. IEEE Medical Imaging Conf.*, Anaheim, CA, Nov. 1996.
[26] K. Ramchandran and M. Vetterli, "Best wavelet packet bases in a rate-distortion sense," *IEEE Trans. Image Processing*, vol. 2, pp. 160–175, April 1993.

[27] K. Ramchandran, Z. Xiong, K. Asai, and M. Vetterli, "Adaptive transforms for image coding using spatially-varying wavelet packets," *IEEE Trans. Image Processing*, vol. 5, pp. 1197–1204, July 1996.

[28] O. Rioul and M. Vetterli, "Wavelet and signal processing," *IEEE Signal Processing Mag.*, pp. 14–38, Oct. 1991.

[29] N. Saito and G. Beylkin, "Multiscale representations using the auto-correlation functions of compactly supported wavelets," *IEEE Trans. Signal Processing*, vol. 41, pp. 3584–3590, Dec. 1993.

[30] M. J. Shensa, "The discrete wavelet transform: Wedding the a trous and Mallat algorithms," *IEEE Trans. Signal Processing*, vol. 40, pp. 2464–2482, Oct. 1992.

[31] Z. Shi and Z. Bao, "Group-normalized processing of complex wavelet packets," *Sci. China (E)*, vol. 26, no. 12, 1996.

[32] ——, "Group-normalized wavelet packet signal processing," *Proc. SPIE*, vol. 3078, pp. 226–239, Apr. 1997.

[33] ——, "Fast image coding of interval interpolating wavelets," *Proc. SPIE*, vol. 3078, pp. 240–253, Apr. 1997.

[34] Z. Shi, D. J. Kouri, G. W. Wei, and D. K. Hoffman, "Generalized symmetric interpolating wavelets," *Comput. Phys. Commun.*, vol. 119, no. 2/3, pp. 194–218, June 1999.

[35] Z. Shi, G. W. Wei, D. J. Kouri, and D. K. Hoffman, "Perceptual normalized subband image restoration," in *Proc. IEEE Symp. Time-Frequency Time-Scale Analysis*, Pittsburgh, PA, Oct. 1998, N. 144, pp. 469–472.

[36] ——, "Visual group normalization using Gaussian–Lagrange distributed approximating functional wavelets," *IEEE Signal Processing Lett.*, submitted for publication.

[37] W. Swelden, "The lifting scheme: A custom-design construction of biorthogonal wavelets," *Appl. Comput. Harmon. Anal.*, vol. 3, no. 2, pp. 186–200, 1996.

[38] T. D. Tran and R. Safranek, "A locally adaptive perceptual masking threshold model for image coding," in *Proc. IEEE ICASSP*, 1996, pp. 1882–1885.

[39] M. Unser, A. Adroubi, and M. Eden, "The L_2 polynomial spline pyramid," *IEEE Trans. Pattern Anal. Machine Intell.*, vol. 15, pp. 364–379, Apr. 1993.

[40] P. Vaidyanathan and T. Chen, "Role of anti-causal inverse in multirate filter-banks—Part I: System-theoretic fundamentals," *IEEE Trans. Signal Processing*, vol. 43, pp. 1090–1102, May 1995.

[41] P. Vaidyanathan and T. Chen, "Role of anti-causal inverse in multirate filter-banks—Part II: The FIR case, factorizations, and biorthogonal lapped transforms," *IEEE Trans. Signal Processing*, vol. 43, pp. 1103–1115, May 1995.

[42] M. Vetterli and C. Herley, "Wavelet and filter banks: Theory and design," *IEEE Trans. Signal Processing*, vol. 40, pp. 2207–2232, Sept. 1992.

[43] J. D. Villasenor, B. Belzer, and J. Liao, "Wavelet filter evaluation for image processing," *IEEE Trans. Image Processing*, vol. 4, pp. 1053–1060, Aug. 1995.

[44] A. B. Watson, G. Y. Yang, J. A. Solomon, and J. Villasenor, "Visibility of wavelet quantization noise," *IEEE Trans. Image Processing*, vol. 6, pp. 1164–1175, Aug. 1997.

[45] G. W. Wei, D. S. Zhang, D. J. Kouri, and D. K. Hoffman, "Lagrange distributed approximating functionals," *Phys. Rev. Lett.*, vol. 79, no. 5, pp. 775–779, 1997.

[46] G. W. Wei, D. J. Kouri, and D. K. Hoffman, "Wavelets and distributed approximating functionals," *Phys. Rev. Lett.*, submitted for publication.

[47] X.-G. Xia and Z. Zhang, "On sampling theorem, wavelets and wavelet transforms," *IEEE Trans. Signal Processing*, vol. 41, pp. 3524–3535, Dec. 1993.

[48] Z. Xiong, K. Ramchandran, and M. T. Orchard, "Space-frequency quantization for wavelet image coding," *IEEE Trans. Image Processing*, vol. 6, pp. 677–693, May 1997.

[49] S. H. Zhang *et al.*, "Target extraction from strong clutter background," Tech. Rep., Nat. Key Lab. Radar Signal Processing, Xidian Univ., 1994.

Zhuoer Shi (M'98), photograph and biography not available at time of publication.

G. W. Wei, photograph and biography not available at time of publication.

Donald J. Kouri (M'98), photograph and biography not available at time of publication.

David K. Hoffman, photograph and biography not available at time of publication.

Zheng Bao (SM'88), photograph and biography not available at time of publication.